

Machine learning for Thermal Modelling of Metal Additive Manufacturing Processes

Jagadeeswaran Murapaka

A Dissertation Submitted to
Indian Institute of Technology Hyderabad
In Partial Fulfillment of the Requirements for
The Degree of Master of Technology



भारतीय प्रौद्योगिकी संस्थान हैदराबाद
Indian Institute of Technology Hyderabad

Department of Interdisciplinary (Additive Manufacturing)

June, 2024

Declaration

I declare that this written submission represents my ideas in my own words, and where others' ideas or words have been included, I have adequately cited and referenced the original sources. I also declare that I have adhered to all principles of academic honesty and integrity and have not misrepresented or fabricated or falsified any idea/data/fact/source in my submission. I understand that any violation of the above will be a cause for disciplinary action by the Institute and can also evoke penal action from the sources that have thus not been properly cited, or from whom proper permission has not been taken when needed.



(Signature)

Jagadeeswaran Murapaka

AM22MTECH14001

Approval Sheet

This thesis entitled **Machine Learning approach for Thermal Modelling of Metal Additive Manufacturing Processes** by JAGADEESWARAN MURAPAKA is approved for the degree of Master of Technology from IIT Hyderabad.



Dr. Gopinath Muvvala

Department of Mechanical and Aerospace Engineering

Indian Institute of Technology, Hyderabad

Examiner

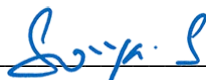


Dr. Rajesh Korla

Department of Material science and Metallurgical Engineering

Indian Institute of Technology, Hyderabad

Examiner



Prof. Suryakumar S.

Department of Mechanical and Aerospace Engineering

Indian Institute of Technology, Hyderabad

Adviser

Acknowledgements

I would like to express my special thanks of gratitude to my supervisor **Prof. Suryakumar S.**, Indian Institute of Technology, Hyderabad for giving me the golden opportunity to carry out this project and provide me the constant guidance throughout this work. I would also like to express my deep sense of thanks to my co-adviser **Dr. Saketha Nath Jagarlapudi** for providing me with the directions in my project. It was a great privilege and honor to work under their guidance.

I would like to thank my fellow lab mates: Nagallpatti Vishwanath, Vishnu S, Rahul John, Ashutosh, Pranav, Siddharth and Aravind for the discussions during weekly meetings.

Abstract

Machine learning, a rapidly advancing field, plays a significant role in additive manufacturing, a technology still in its development stages. Within the realm of large-scale additive manufacturing, Wire Arc Additive Manufacturing (WAAM) stands out due to its high deposition rate, wide material selection, and substantial productivity. However, WAAM faces challenges with residual stresses caused by large thermal gradients, which can distort the final product. To address this issue, Thermal modelling forms a basis to understand the thermal behavior of the part and helps in study of heat distribution and accumulation during the process which in turns are the major causes of residual stresses and distortion. This work aims to explore Data driven ML and Physics informed machine learning model (PIML), specifically physics informed Neural Networks (PINNs) for thermal modelling without or with very limited simulated data by incorporating the process physics.

Physics-Informed Neural Networks integrate the governing equations of heat transfer and their boundary conditions. This integration merges the reliability of physics-based models with the adaptability of neural networks, enabling real-time prediction of temperature distribution. This thesis delves into the expectations and potential of machine learning in enhancing additive manufacturing, particularly focusing on its future impact and significance.

Abbreviations

- WAAM Wire Arc Additive Manufacturing
- AM Additive Manufacturing
- ML Machine learning
- DED Direct Energy Deposition
- CNC Computer Numerical Control
- CMT Cold Metal Transfer
- PINN Physics Informed Neural Networks
- L-DED – Laser Directed energy deposition

Contents

Approval Sheet.....	iii
Acknowledgements.....	iv
Abstract.....	v
Abbreviations	vi
Contents.....	vii
Chapter 1: Introduction.....	1
1.1 Directed Energy Deposition.....	1
1.2 Necessity of Machine Learning	2
1.3 Physics Informed Neural Networks (PINNs).....	4
1.4 Working of PINN.....	6
Chapter 2: Literature Review.....	8
2.1 Thermal Modelling of WAAM	8
2.2 Contributions in PIML and Applied PINNs.....	13
Chapter 3: Problem Definition.....	20
3.1 Problem definition and Methodology	20
3.2 ML for AM: Data Driven Approach.....	21
3.2.1 Model Architecture.....	22
3.2.2 Training Process.....	24
3.2.3 Model Evaluation.....	24
3.2.3.1 Sequential Actual Temperature-Based Prediction.....	24
3.2.3.2 Sequential Iterative Prediction.....	25
3.3: ML For AM: PINN Approach	26
3.3.1 Governing Equations.....	26
3.3.2 Assumptions for the study.....	27
3.3.3 Boundary conditions.....	27

3.3.4. Implementation of PINN model.....	28
3.3.4.1 Example Problem on Laser Material Processing.....	28
3.3.4.2 3D Transient Thermal Analysis on Laser -DED.....	30
3.3.4.3 3D Transient Thermal Analysis on WAAM.....	36
3.3.4.4 3D Transient Thermal Analysis considering Temperature Dependent Properties on WAAM.....	41
3.3.4.5 Hybrid PINN model Applied on WAAM.....	43
3.4 Discussions.....	46
Chapter 4: Future Work.....	48
References.....	50

List of Figures

1. Figure 1.1: Schematic of WAAM [1]	1
2. Figure 1.2: Schematic of Laser Powder DED [2]	2
3. Figure 1.3: Typical architecture of Recurrent Neural Network (RNN) [3].....	4
4. Figure 1.4 Workflow of PINN [4]	6
5. Figure 2.1: Thermal modelling in FEM and thermal cycle of multi-layer build [5]	9
6. Figure 2.2: Goldak double ellipsoidal heat source [6]	9
7. Figure 2.3: (a) The double ellipsoid heat source model and (b) Proposed Droplet Volume approach in WAAM [6].....	10
8. Figure 2.4: Difference of melt pool cross sections b/w arc welding and WAAM [6]..	10
9. Figure 2.5: 3D Finite element model [7].....	11
10. Figure 2.6: Comparison of Simulation & Experimental results [7].....	12
11. Figure 2.7: Comparison of Temperature Gradients [7]	12
12. Figure 2.8: From left to right: epidermis, dermis, and fat [8].....	13
13. Figure 2.9: Predicted Temperature using different activation functions [8].....	14
14. Figure 2.10(a): Convective heating of a part [10].....	15
15. Figure 2.10(b): Comparison between PINN, FEM and Data driven ML[10].....	15
16. Figure 2.11 Predicted temperature by PINN (b) FEM solution (c) Absolute Error [11].....	16
17. Figure 2.12: Hybrid PINN Workflow [13]	18
18. Figure 2.13: Comparison analysis of predicted data and measured IR data [13]	19
19. Figure 3.1: Schematic of Deep Neural network Architecture [14]	20
20. Figure 3.2 : Methodology of working model	22
21. Figure 3.3 : Interface of simufact welding software.....	22

22. Figure 3.4: (a) Zigzag Horizontal pattern (b) Zigzag Vertical Pattern	23
23. Figure 3.5: (a) Contour Pattern considered for testing (b) Comparison of Predicted and actual temperature at Top left corner point (-103.95, 24.75).....	24
24. Figure 3.6 Time- temp Prediction at top left point (-103.95, 24.75)	26
25. Figure 3.7 Schematic of Process physics with Boundary condition of Metal Additive process [15]	27
26. Figure 3.8 (a) 3D Latin hypercube sampling of Domain (b) Loss curves.....	29
27. Figure 3.9 Model predictions at t= 0.1, 0.2 and 0.3 sec.....	29
28. Figure 3.10 (a) 2D Top surface (b) 3D custom sampling strategy of domain.....	32
29. Figure 3.11 PINN Architecture Followed.....	33
30. Figure 3.12 (a) 3D model Predictions at t= 0, 1, 2, 3 sec (b) Comparison analysis of model predictions with simulation results.....	34
31. Figure 3.13 (a) Loss curves (b) Error analysis.....	35
32. Figure 3.14: Goldak Double Ellipsoidal Heat Source [16]	37
33. Figure 3.15(a): 2D Top surface sampling (b) 3D domain and Boundary sampling	38
34. Figure 3.16(a): 3D model Predictions at t= 0, 1, 2, 3 sec (b) Comparison analysis of model predictions with simulation results.....	39
35. Figure 3.17: (a) Loss curves (b) Error analysis.....	40
36. Figure 3.18: (a) 3D model Predictions at t= 0, 1, 2, 3 sec (b) Comparison analysis of model predictions with simulation results	41
37. Figure 3.19 (a) Loss curves (b) Error analysis	42
38. Figure 3.20 (a) 3D model Predictions at t= 0, 1, 2, 3 sec (b) Comparison analysis of model predictions with simulation results.....	44
39. Figure 3.21 (a) Loss curves (b) Error analysis.....	45

List of Tables

Table 3.1: Process parameters and material Properties considered for.....	23
Table 3.2: Model Training and NN parameters	24
Table 3.3: Process parameters and Material properties for L-DED.....	32
Table 3.4: PINN Network Parameters for L-DED	33
Table 3.5: Goldak Double ellipsoidal Heat source parameters	37
Table 3.6: Process, material and Model parameters for WAAM.....	39
Table 3.7: Hybrid Model parameters for WAAM	44

Chapter 1

Introduction

1.1 Directed Energy Deposition

Directed Energy Deposition (DED) is a method in additive manufacturing (AM) that utilizes materials in the form of wire or powder. This material is melted using a heat source such as a laser, electric arc, or electron beam, and then deposited layer by layer. Among the various DED techniques, Wire Arc Additive Manufacturing (WAAM) and Laser DED are currently the most popular. WAAM, a specific type of DED, uses an electric arc as the heat source and wire as the feedstock. The welding torch's movement is controlled by a CNC setup or a robot, with the wire being continuously supplied through a wire feed system. WAAM is especially effective at producing components that are nearly in their final shape.

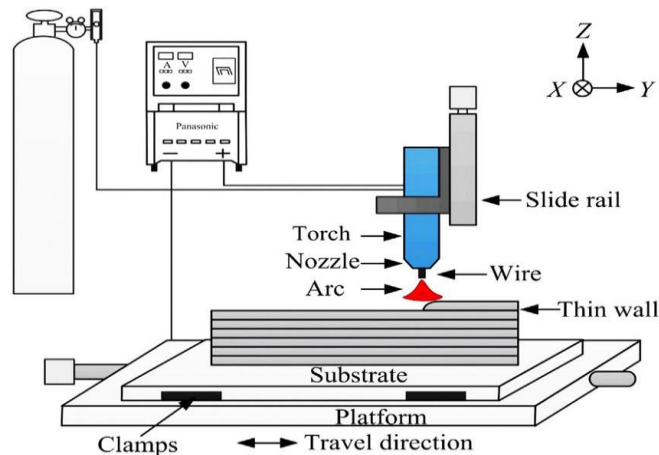


Fig 1.1. Schematic of Wire arc AM Process [1]

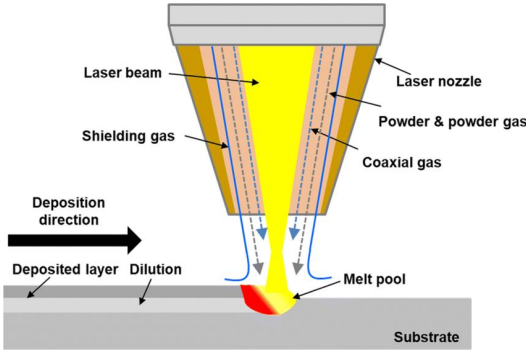


Fig1.2. Schematic of Laser Powder DED [2]

While WAAM offers numerous benefits, it commonly faces challenges such as residual stress and distortion. These issues arise due to the significant temperature differences, thermal strain, and residual stress that occur when a new layer is deposited on a cooler substrate or on a previously deposited layer. Such residual stresses can adversely affect the fatigue life and fracture toughness of the component, leading to problems like distortion, reduced geometric accuracy, and layer separation during the deposition process.

There are several techniques to mitigate residual stress in WAAM. These include preheating the substrate, using shorter deposition paths or depositing in smaller segments, employing effective deposition patterns such as inward spiraling, increasing the scanning speed, and reducing the height of each deposited layer. Notably, preheating the substrate can significantly reduce the stress developed during fabrication and the final residual stress. High preheating temperatures help in diminishing the strain by reducing the temperature differential and, consequently, the thermal strain. Moreover, this approach can also be beneficial in lowering the likelihood of solidification cracking. Adjusting the power and scanning speed are other viable methods to curtail residual stresses in the process.

1.2 Necessity of Machine Learning

From literature, it is well known that simulations are computationally intensive. Therefore, machine learning models offer a viable alternative for faster prediction of thermal data with reasonable accuracy. The objective of this study is to develop

a generic model that leverages machine learning for efficient thermal data prediction. This involves programming a machine to use data, past experiences, or differential equations, particularly in the case of Physics-Informed Neural Networks (PINNs), to optimize its performance for specific tasks. Machine learning can be applied in various fields, including medical, banking, and engineering applications.

Different machine learning algorithms such as Linear Regression, Logistic Regression, Decision Trees, and Support Vector Machines (SVM) can be utilized. Artificial Neural Networks (ANNs) are particularly noteworthy due to their analogy with human brains. ANNs can learn complex patterns and make accurate predictions. These computational models consist of interconnected nodes called neurons, organized into layers. Each neuron in one layer is connected to neurons in the subsequent layer. The layers are typically classified into three types: Input layer, Hidden layer, and Output layer. The schematic of an ANN is shown in

Recurrent Neural Networks (RNNs) are especially useful for sequential modeling, such as the thermal modeling of the Wire Arc Additive Manufacturing (WAAM) process. RNNs are designed to recognize patterns in sequences of data, making them ideal for time-dependent processes. In the context of WAAM, RNNs can effectively capture the temporal dependencies and dynamics of thermal data over time, allowing for more accurate and robust predictions of thermal behavior throughout the manufacturing process.

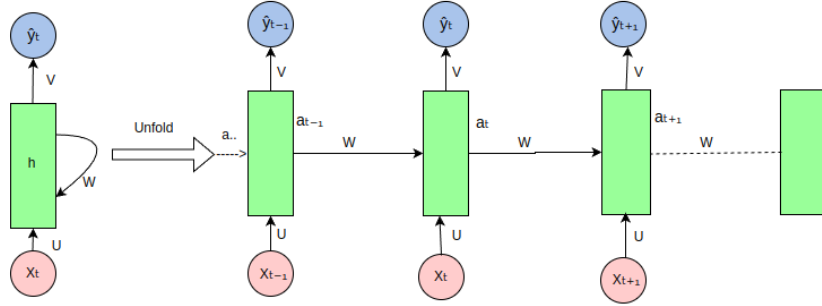


Fig1.3 Typical architecture of Recurrent Neural Network (RNN) [3]

Technically, RNNs process sequences by maintaining a hidden state vector that is updated at each time step based on the current input and the previous hidden state. This allows RNNs to retain information about previous time steps, making them adept at modeling temporal sequences. For the WAAM process, RNNs can be trained using time-series data of thermal measurements, with the input at each time step being features such as temperature, heat source parameters, and material properties. The hidden layers in RNNs can capture complex temporal relationships and dependencies within the thermal data, enabling the model to make predictions about future thermal states. Advanced variants of Recurrent Neural Networks (RNNs), like Long Short-Term Memory (LSTM) networks and Gated Recurrent Units (GRUs), improve performance by tackling issues such as vanishing gradients. These networks offer more stable and accurate predictions over longer sequences. This sequential modeling capability of RNNs makes them a valuable tool for optimizing thermal management and overall quality in WAAM processes.

1.3 Physics informed Neural Networks (PINNs)

Physics-Informed Neural Networks (PINNs) are a category of machine learning models that integrate physical principles, such as differential equations and boundary conditions, into neural network frameworks. The goal of PINNs is to merge the capabilities of deep learning with the underlying equations of a physical system, thereby enabling precise predictions and the exploration of previously unknown physical phenomena. The primary components of PINNs include:

- Neural Network Architecture: This is composed of layers of neurons interconnected to process and modify input data. The architecture can vary depending on the specific problem and the intricacy of the physical system being simulated.
- Physics-Informed Loss Function: This coalesces different types of losses in order to satisfy the physics of the problem subjected to certain boundary constraints
- Differential Equation Representation: Differential equation is the basis for the physics behind the phenomena. It captures the relation between the solution and input variable through certain derivate components. PINN is formulated to approximate the solution by considering this Differential equation as the physics of the problem
- Boundary and Initial Conditions: These boundary conditions act as the additional constraints to be satisfied along the Differential equation during training. The boundary conditions may be of Dirichlet, Neumann, Robin type. PINN should be able to incorporate these BC and IC's during training and ensure the predictions are aligned with prescribed Boundary and Initial conditions.
- Collocation Points Utilization: These are the points located within the domain which are used to train the PINN to satisfy the governing equation.

Physics informed neural networks uses Automatic differentiation technique using Pytorch or TensorFlow for developing the components to form the governing equation.

1.4 Working of PINN

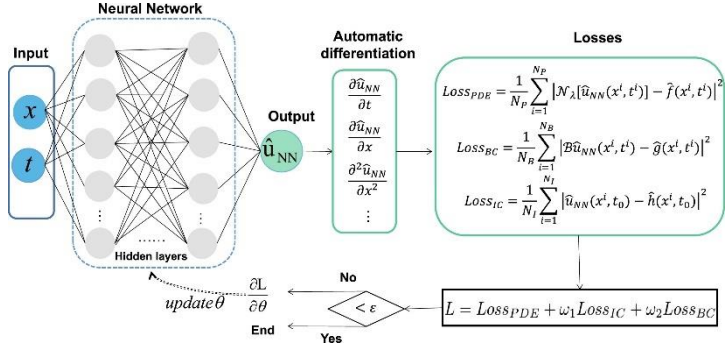


Fig1.4 Workflow architecture of PINN [4]

Domain:

- We consider PDEs in numerical simulations within a bounded domain.

$$\text{Let } \tilde{\Omega} = \Omega \times [0, T] \text{ where } \Omega \subset \mathbb{R}^d \text{ and } d \in \mathbb{N} \quad \text{----- Eq. 1}$$

Initial and Boundary conditions:

$$\text{The boundary is defined as } \partial\Omega = \partial\tilde{\Omega} \times (0, T) \cup \Omega \times \{0\} \quad \text{----- Eq. 2}$$

- This implies that numerically, the boundary and initial data are treated equally.

Formation of PDE

- For a point $x = (x_1, \dots, x_d, t)^T \in \tilde{\Omega}$, we consider a PDE.
- The PDE with solution $u: \tilde{\Omega} \rightarrow \mathbb{R}$ is denoted as:

$$f(x, D^{k_1}u, \dots, D^{k_m}u) = 0, \text{ for } x \in \tilde{\Omega}. \quad \text{----- Eq. 3}$$

$$\mathcal{B}(u, x) = 0, \quad x \in \partial\tilde{\Omega}. \quad \text{----- Eq. 4}$$

Training Process of PINN

- Construct Neural network which acts as surrogate solution for u

Let $u^\Theta: \mathbb{R}^d \rightarrow \mathbb{R}$ be a Feedforward Neural Network (FNN):

2. Define your Domain and PDE:

Let $u: \tilde{\Omega} \rightarrow \mathbb{R}$ be the solution of the PDE given by $f(x, D^{k_1}u, \dots, D^{k_m}u) = 0$

Where

$$D^k u = \partial_{x_1}^{k_1} \cdots \partial_{x_d}^{k_d} \quad \text{----- Eq. 5}$$

3. Initial and Boundary conditions:

The boundary and initial conditions are defined as $B(u, x) = 0$ for $x \in \tilde{\Omega}$.

4. PINN Loss functions:

For given sets of training points $T_f \subset \tilde{\Omega}$ and $T_b \subset \partial\tilde{\Omega}$, the PINN loss

$L_T : \mathbb{R}^\mu \rightarrow \mathbb{R}$ is defined as

$$\mathcal{L}_T(\Theta) = w_f \mathcal{L}_{T_f}(\Theta) + w_b \mathcal{L}_{T_b}(\Theta) \quad \text{----- Eq. 6}$$

Where,

$$\begin{aligned} \mathcal{L}_{T_f}(\Theta) &= \frac{1}{|T_f|} \sum_{x \in T_f} \|f(x, D^{k_1}\hat{u}, \dots, D^{k_m}\hat{u})\|_2^2, \\ \mathcal{L}_{T_b}(\Theta) &= \frac{1}{|T_b|} \sum_{x \in T_b} \|B(\hat{u}, x)\|_2^2 \end{aligned} \quad \text{----- Eq. 7}$$

w_f, w_b are the weights that force PINN to perform optimization by taking these as importance of PDE residual and Boundary residual respectively.

Chapter 2

Literature Review

2.1 Thermal Modelling of WAAM

Understanding heat transport, solidification behavior, and the associated residual stresses and distortion is essential for robust thermal modeling of metal additive manufacturing. This modeling forms the foundation for conducting these studies. Heat source model with uniform distribution offers significant benefits in processing time due to its insensitivity to mesh configuration. Validating the model's simulated temperature profiles and distribution against experimental measurements from thermocouples and a high-temperature thermal imaging camera instills confidence in its accuracy.

Edison et al. [5] investigated the effects of multi-layered deposition on the estimation and confirmation of melt pool shapes and thermal processes. Their study utilized finite element analysis to account for heat dissipation due to convection and radiation on the surfaces of the additive manufacturing layers. They employed the element birth and death method to simulate the additive layering of continuous wire, adding various elements to form rectangular builds on the base material. A 3D transient nonlinear heat transfer analysis was conducted to predict temperature variations during the entire welding and cooling phases, including the base substrate and two to three layers of cast IN-738LC alloy. Figure 2.1 illustrates the predicted thermal contours and the temperature cycles at specific nodes.

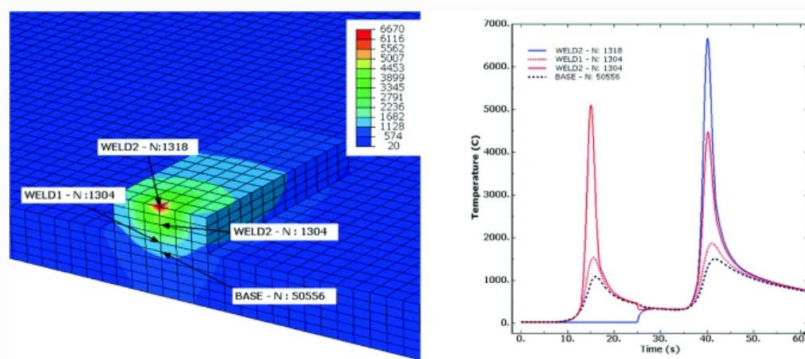


Fig 2.1. Thermal modelling in FEM and thermal cycle of multi-layer built [5]

R.F.V. Sampaio [6], reported that the double ellipsoid heat source model proposed by Goldak et al. is frequently utilized in the finite element method (FEM) analysis of WAAM, as illustrated in the figure 2.2.

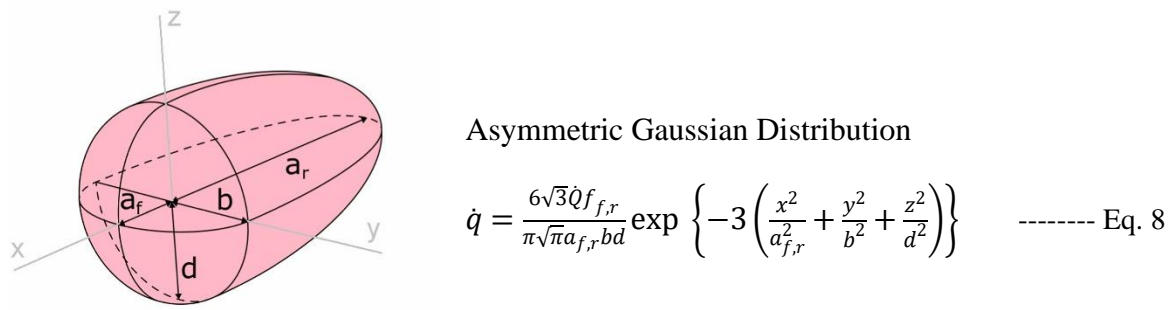


Fig 2.2 Goldak double ellipsoidal heat source [6]

Where,

b = half width mm d = Depth of weld pool mm a_f, a_r = Semi axis length mm (front and rear)

Graf et al.[6] and Ahmad et al.[6] discovered that in certain instances, the temperatures calculated using the aforementioned heat source model can exceed the evaporation temperature. To address this, they suggest modifying the intensity parameter in the equation.

To solve this issue, Montevercchi et al [6]. proposed a three-fold solution

- Dividing heat input Q equally between base Q_b and filler Q_w .
- Applying double ellipsoid power density \dot{q}_b for the base, substituting \dot{Q} with \dot{Q}_b .
- Use a constant power density distribution $\dot{q}_w = \frac{\dot{Q}_w}{V_{el}}$ for the filler

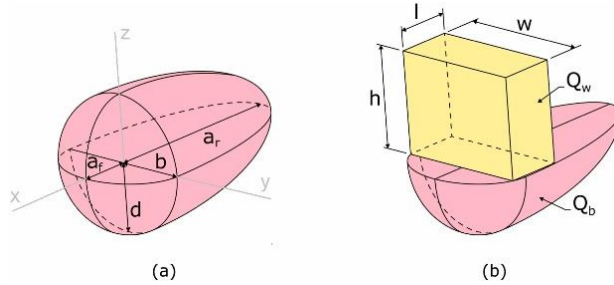


Fig. 2.3 (a) The double ellipsoid heat source model and (b) Proposed Droplet Volume approach in WAAM [6].

Droplet volume $V_{el} = l * w * h$ is represented as a box where heat \dot{q}_v is applied to simulate deposition and melting.

Mohebbi et al.,[6] suggests that the differences in the melt pool cross sections of arc welding and WAAM should inevitably give rise to differences in the melting efficiency of both processes due to differences in the heat transferred to the solid metal and lost to the environment. In particular, the approximate semi-infinite plate heat transfer conditions of arc welding are different from the approximate one-dimensional heat transfer conditions of material deposition in WAAM.

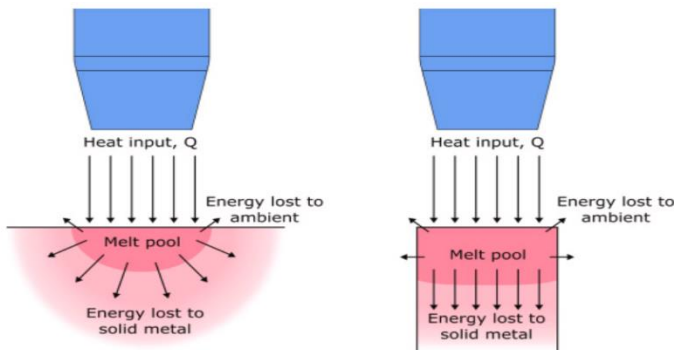


Fig. 2.4 Difference of melt pool cross sections between arc welding and WAAM [6]

Huihui et al.,[7] have investigated the thermal behaviour of a ten-layer single-pass deposition. A 3D transient heat transfer simulation that accounts for temperature-dependent material properties has been conducted to assess the development of the temperature field, the characteristics of thermal cycling, temperature gradients, and the influence of deposition directions on the thermal dynamics of single-pass, ten-layer rapid prototyping. The simulation results align closely with experimental data. The research suggests that the condition for heat dispersion in the melt pool worsens with increasing deposition height. However, maintaining other conditions constant, optimizing the direction of deposition can significantly improve heat dispersion. It is found that consistent deposition directions result in better heat diffusion compared to alternating directions. Although rapid prototyping using welding shares the same heat source as conventional welding, notable differences in thermal processes exist, which include:

- Variations in the ratio of volume,
- Distinct thermal cycles,
- Unique key issues specific to the process,
- Varied paths of deposition.

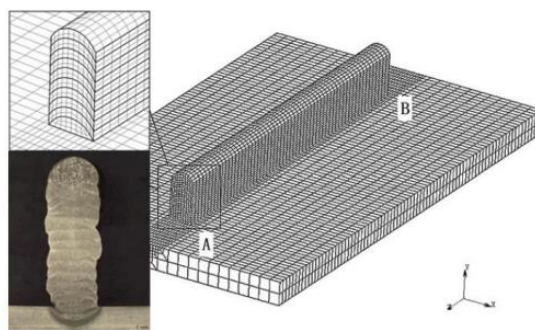


Figure 2.5 3D Finite element model [7].

Figure 2.5 presents a 3D finite element model with a focus on points A and B. In Figure 2.6, there are two types of lines: the actual line, representing data measured by

a thermocouple, and a dashed line, depicting the modeled thermal cycle curve. This information is illustrated below.

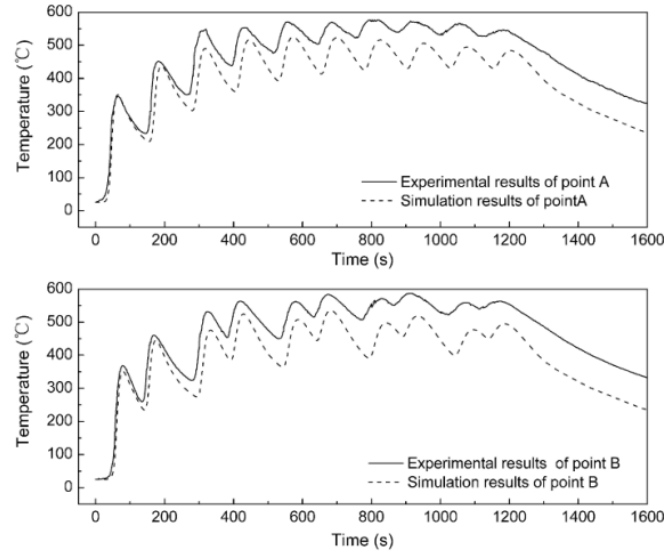


Figure 2.6 Comparison of Simulation & Experimental results [7]

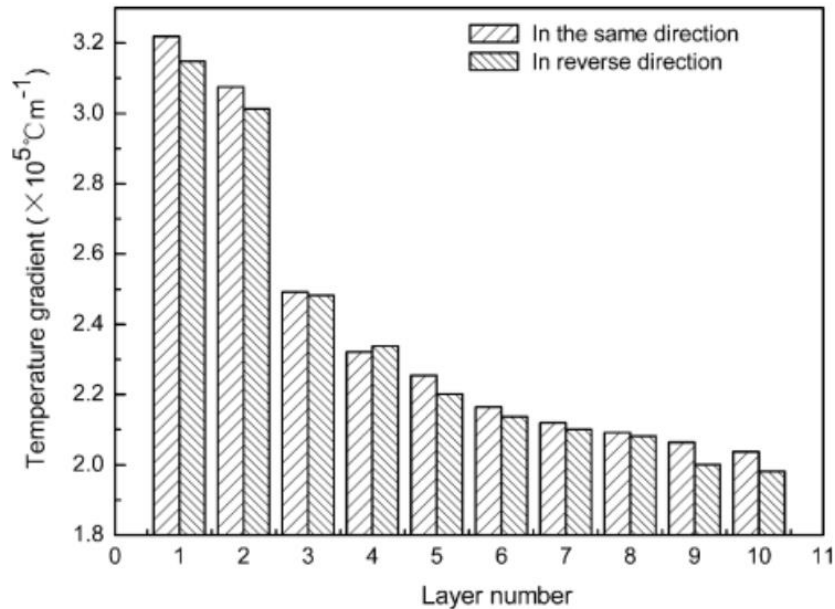


Figure 2.7 Comparison of Temperature Gradients [7]

They also investigate the impact of the fabrication pattern on the temperature gradient. The study notes that as the height of deposition increases, resulting in greater heat loss, the temperature gradient within the molten pool decreases. In the context of

weld-based rapid prototyping, it is observed that the temperature gradient is more pronounced when depositing in the same direction compared to the reverse direction. This observation is depicted in Figure 2.7.

2.2 Contributions in PIML and applied PINNs

Lagaris et al.,[9] proposed ANN's for solving differential equations

$$G(\vec{x}, \Psi(\vec{x}), \nabla\Psi(\vec{x}), \nabla^2\Psi(\vec{x})) = 0, \vec{x} \in D \quad \text{----- Eq. 9}$$

Under specific boundary conditions (BCs), such as Dirichlet and/or Neumann conditions, Domain D and its boundary S can be divided into a set of points D and S , respectively. The problem is then turned into the following system of equations:

$$G(\vec{x}_i, \Psi(\vec{x}_i), \nabla\Psi(\vec{x}_i), \nabla^2\Psi(\vec{x}_i)) = 0, \forall \vec{x}_i \in \widehat{D} \quad \text{----- Eq. 10}$$

If $\Psi_t(\vec{x}, \vec{p})$ represents the trial solution that has adjustable parameters \vec{p} , the problem is converted to:

$$\min_{\vec{p}} \sum_{\vec{x}_i \in D} \left(G(\vec{x}_i, \Psi_t(\vec{x}_i, \vec{p}), \nabla\Psi_t(\vec{x}_i, \vec{p}), \nabla^2\Psi_t(\vec{x}_i, \vec{p})) \right)^2 \quad \text{----- Eq. 10}$$

Proposed Method:

$$\Psi_t(\vec{x}) = A(\vec{x}) + F(\vec{x}, N(\vec{x}, \vec{p})) \quad \text{----- Eq. 11}$$

- $A(\vec{x})$ contains no tweakable parameters and satisfies the BC's.
- where $N(\vec{x}, \vec{p})$ is a single-output FFNN with parameters \vec{p} and n input units fed with the input vector \vec{x} .

Brett Bowman et al. [8] applied PINNs to a 1-D Advection–Diffusion–Reaction equation modeling laser energy interaction with skin tissue.



Fig 2.8: From left to right: epidermis, dermis, and fat [8]

They suggested that random sampling is best choice than Latin Hypercube sampling in case of presence of heat source term and strictly suggested that Hybrid activation and Tanh activation functions might be most effective for PDEs with source terms in PINN models.

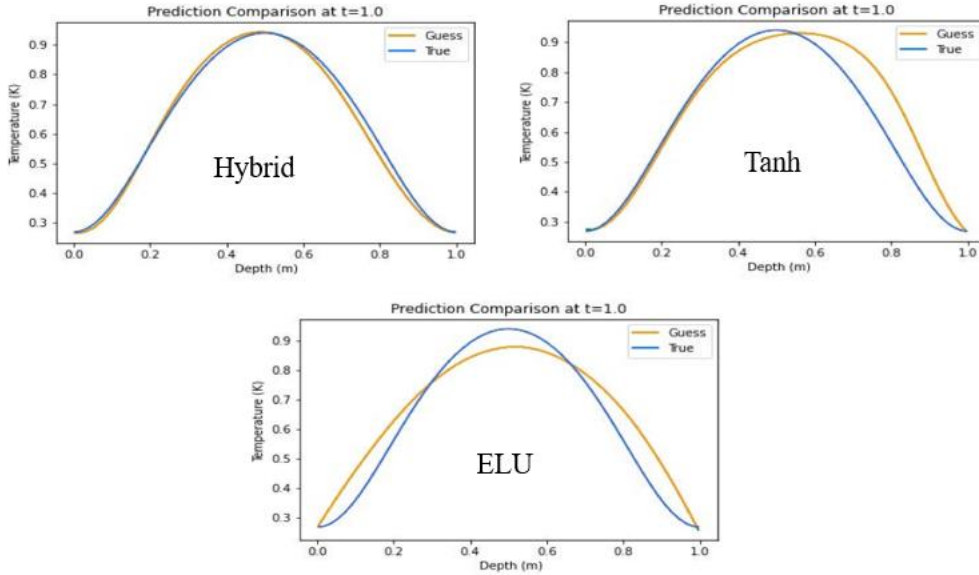


Fig 2.9: Predicted Temperature using different activation functions [8]

Navid et al. [10] developed a method to solve the conductive heat transfer partial differential equation (PDE) by incorporating it with convective heat transfer PDEs as boundary conditions. As illustrated in Figure after 50,000 training iterations, the model's predictions for the central part of the object are compared with those derived from Finite Element (FE) analysis. All network models consistently and accurately predict temperature patterns within the trained area. However, shortly after exiting this trained area, all model solutions start to deviate from the FE analysis. To accurately represent physics beyond the trained zone, only the Physics-Informed Neural Network (PINN) with physics-informed activation functions proves effective. This effectiveness is attributed to PINN's use of physics-informed functions, which more precisely replicate the dynamics of heat transfer in the problem.

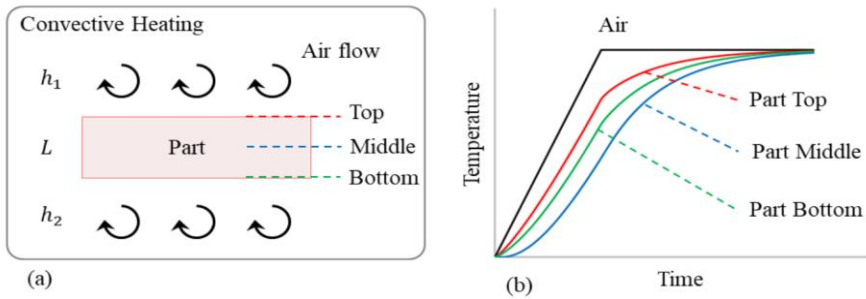


Fig 2.10 (a): Convective heating of a part [10]

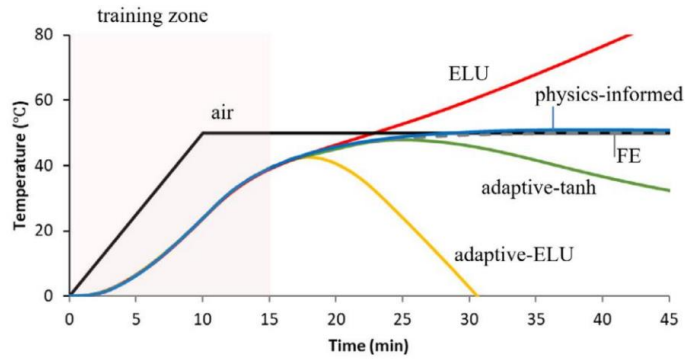


Fig 2.10 (b): Comparison between PINN, FEM and Data driven ML [10]

The accuracy of the trained Physics-Informed Neural Network (PINN) was verified in various one-dimensional and two-dimensional heat transfer scenarios by comparing its predictions to Finite Element (FE) analysis data. The performance and precision of PINN were also evaluated against a traditional Neural Network (NN) that lacked feature engineering. The results showed that both NN and PINN align with FE data within the training domain, but only PINN equipped with engineering features can accurately forecast results outside this domain by effectively capturing the underlying physical principles of the problem.

Jorrit Voigt and colleagues [11] created a model for dynamic three-dimensional heat transfer in laser material processing, employing Physics-Informed Neural Networks (PINNs). Their model addresses dynamic heat conduction in bulk materials, which is described by the time-dependent heat conduction equation, a partial differential equation involving both spatial coordinates \vec{x} and time t

$$c_p \frac{\partial}{\partial t} u(\vec{x}, t) = \frac{\kappa}{\rho} \Delta u(\vec{x}, t) + \dot{Q}(\vec{x}, t) \quad \text{----- Eq. 12}$$

The temperature distribution is modeled within a finite cubic region. A Dirichlet boundary condition (BC) was applied to its lower base, setting the temperature to 0.

For the four lateral faces (F) the Neumann BC was

$$\frac{\partial}{\partial t} u(\vec{x}, t) = 0.1 \quad \text{----- Eq. 13}$$

The initial conditions (IC) were established as $u=0$ throughout the entire domain.

These conditions are inspired by the common setup in the laser powder bed fusion process (PBF-LB/M).

For the heat source a Gaussian beam profile with a laser power $P_L = 1 \text{ W}$ and a velocity of 1 mm/s was used. The heat source is modelled by:

$$\dot{Q} = \frac{2 \cdot P_L}{\pi \cdot r_{\text{spot}}^3} \cdot \exp \left(-2 \cdot \frac{r_{\text{focus}}^2}{r_{\text{spot}}^2} \right) \quad \text{----- Eq. 14}$$

The size of the laser spot (r_{spot}) was 0.1 mm and the position of the laser focus (r_{focus}) was a function of time.

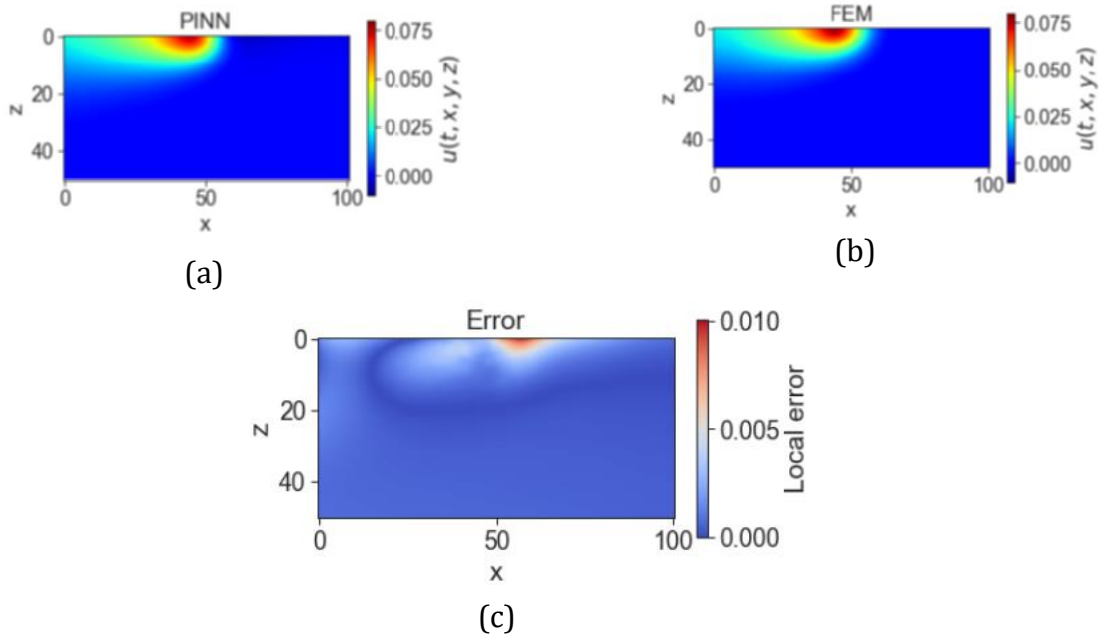


Fig 2.11: (a) Predicted temperature by PINN (b) FEM solution (c) Absolute Error [11]

To reduce the computational load, the approach does not calculate errors from the governing equation at every point in the lattice. Instead, it stochastically samples these errors from a sufficiently dense subset of lattice points, targeting about 20% in each epoch. For the computations, a total of 40,000 collocation points were utilized, selected through the Latin-Hypercube sampling method. This technique helps in efficiently approximating the error distribution while managing the numerical effort required.

Qiming Zhu et al [12] proposed an idea of considering the Dirichlet BC in Hard approach rather than conventional soft approach.

A specific part of the neural network is dedicated to purely satisfying the prescribed Dirichlet boundary conditions (BC).

To achieve this, we first define a Heaviside function as follows:

$$H_\epsilon(\mathbf{x}) = \begin{cases} 1 - \cos[d(\mathbf{x})\pi/\epsilon] & \text{if } d(\mathbf{x}) < \epsilon \\ 1 & \text{if } d(\mathbf{x}) \geq \epsilon \end{cases}$$

$$\mathbf{u}_{NN} = \mathbf{u}_{bc}[1 - H_\epsilon(\mathbf{x})] + \mathbf{u}H_\epsilon(\mathbf{x}) \quad \text{----- Eq. 14}$$

$$p_{NN} = p_{bc}[1 - H_\epsilon(\mathbf{x})] + pH_\epsilon(\mathbf{x})$$

$$T_{NN} = T_{bc}[1 - H_\epsilon(\mathbf{x})] + TH_\epsilon(\mathbf{x})$$

where $d(\mathbf{x})$ = distance to the Dirichlet boundary, ϵ = artificial thickness of the boundary.

The Heaviside function $H_\epsilon(\mathbf{x})$ smoothly transitions from 1 to 0 as $d(\mathbf{x})$ approaches 0. Consequently, the prediction will inherently satisfy the prescribed values by definition, eliminating the need for additional constraints.

Liao et al [13] employed physics-informed neural networks (PINNs) to develop a combined physics-based and data-driven thermal modeling method for additive manufacturing (AM) operations. This approach aims to predict comprehensive temperature histories and identify unknown material and process parameters by

integrating partially observed temperature data from an infrared camera with physical laws.

The hybrid thermal modeling framework for AM, based on PINNs, is illustrated in Figure 2.12

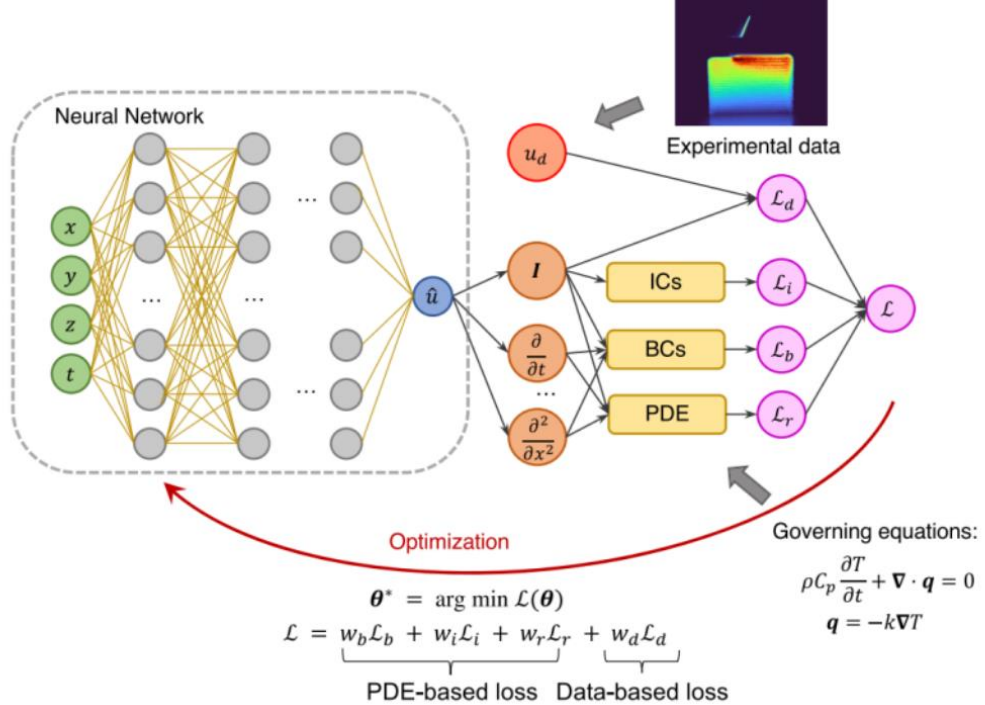


Fig 2.12: Hybrid PINN Workflow [13]

In this workflow, the neural network utilizes spatial-temporal coordinates to predict temperatures at specific locations. The training of the neural network involves a loss function that combines residuals from partial differential equations (PDEs), boundary conditions (BCs), initial conditions (ICs), and an additional data-based loss term incorporating experimental temperature data.

The full-field temperature predictions of the trained Physics-Informed Neural Network (PINN) model are compared with measured infrared (IR) data. The comparison reveals a Root Mean Square Error (RMSE) of 47.28 K between the predicted temperature field and the data measured at $t=7$ seconds, demonstrating the model's accuracy in estimating the total field temperature. This example underscores the effectiveness of the hybrid physics-based data-driven framework in seamlessly

integrating experimental data into the physics-informed model, providing valuable insights into thermal behavior in additive manufacturing (AM) processes.

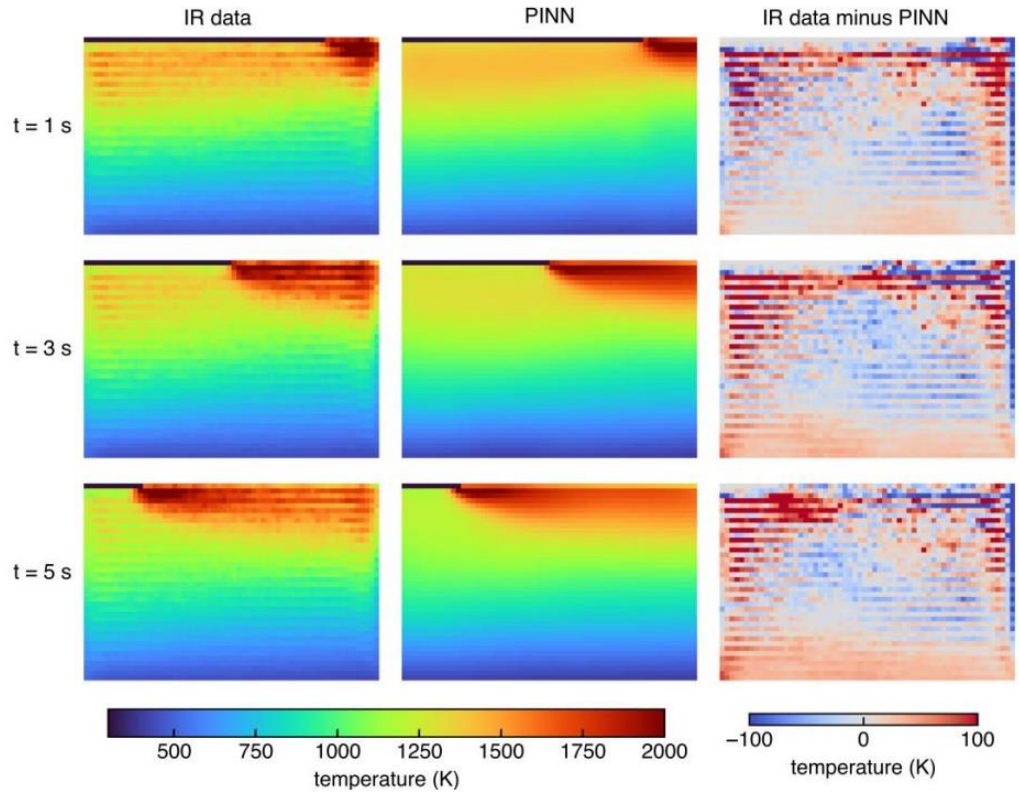


Fig 2.13: Comparison analysis of predicted data and measured IR data [13]

Chapter 3

Problem Definition

3.1 Problem definition and methodology

Problem: Thermal modelling of L-DED and WAAM processes

Objective:

- Is to develop machine learning which can predict the thermal cycles of the process accurately by taking very less time when compared to computationally expensive simulations.

Methodology:

The methodology for this thesis is divided into four stages:

Stage 1: PINN Formulation for Fixed Domain Modelling

- This stage is completed.

Stage 2: Data-Driven ML Approach and Hybrid Model Implementation

- Improvement from Stage 1.
- Hybrid model implementation is in progress.

Stage 3: PINN for Generalized Domain Size Variation

- This stage is planned for future work.

3.2 ML for AM: Data driven approach

Non-uniform thermal gradients can induce residual stress, affecting the microstructure and deteriorating product quality while also causing distortion. Therefore, efficient thermal modeling is crucial to enhance product quality. Traditional experimental approaches and computational simulations are both costly and time-consuming, often requiring extensive effort to predict temperatures for new tool paths.

In our approach ML model addresses these challenges by predicting temperatures based on point coordinates and time. The network is trained for specific tool paths, materials, and domain shapes, enabling accurate temperature predictions for identical configurations. This approach significantly reduces the time and effort needed for thermal modeling, providing a more efficient solution to improve product quality.

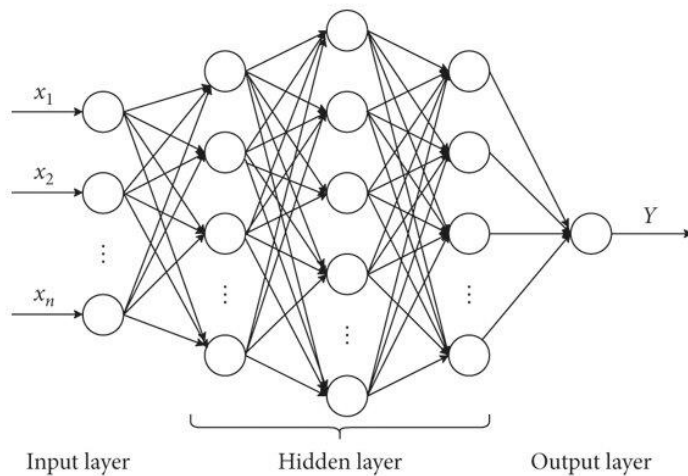


Fig 3.1. Schematic of Deep Neural network Architecture [14]

Developing models that can effectively simulate the thermal behaviour induced by moving heat sources is a significant challenge. To address this, we have employed a Recurrent Neural Network (RNN) architecture in our approach.

To predict the temperature at a given point P at time $t+k$, our method utilizes the temperatures from a 7×7 grid of neighbouring points at time t. The RNN processes this temperature configuration, along with the relative position of the heat source or

torch at times t and $t+k$, to predict the temperature at point P at time $t+k$. By iteratively applying this model at each point P, we can accurately generate the temperature profile of the material throughout the process, accounting for the thermal effects induced by the moving torch.

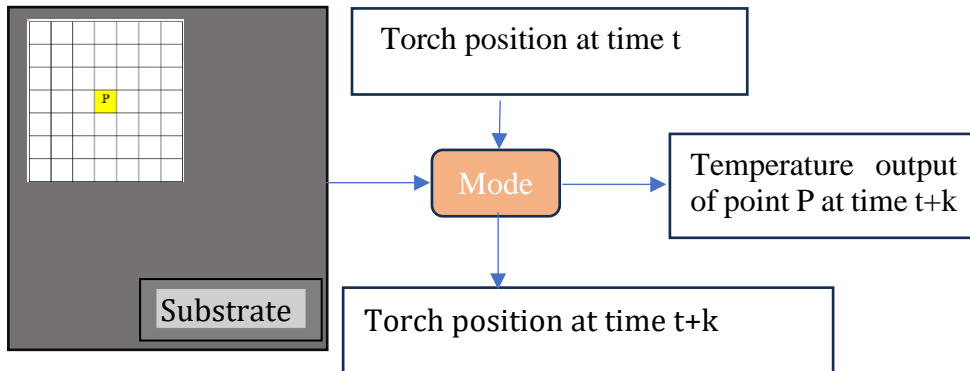
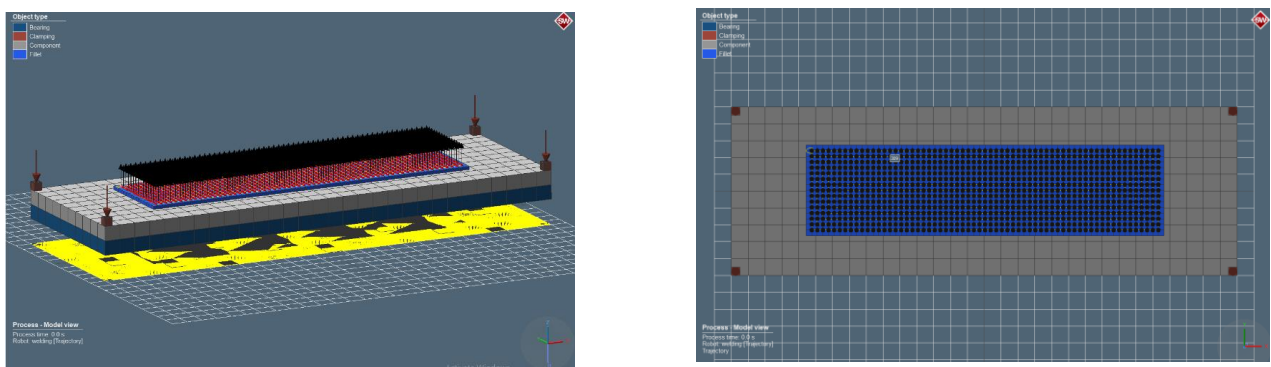


Fig 3.2. Methodology of Working Model

When provided with a new tool path, predicting the temperature is equivalent to evaluating the model. The tool path is the trajectory followed by the heat source during the object printing process. Multiple tool paths can exist for printing the same object. The challenge lies in finding the optimal tool path that minimizes residual stress or distributes residual stress uniformly across the material for a given material, domain shape, and welding shape. The goal is to predict the temperature profile of the material given the tool path and initial temperature profile.

3.2.1. Data Generation:

Abaqus software is used for domain and tool path meshing. **Simufact Welding** is employed to perform simulations, which includes assigning material and heat source parameters and extracting the time-temperature records through post-processing. The simulation generates the temperature profile of the material throughout the process for contour and both zig-zag horizontal and zig-zag vertical patterns.



Process Parameters and Material properties

Category	Parameter	Value
Space and Time Domain	Space and Time Domain	$L*W = 211.2*52.8 \text{ mm}$
	Time Steps	1717
Process Parameters	Current (I)	120 A
	Voltage (U)	15.4 V
	Heat Transfer Efficiency (η)	0.9
	Travel Speed (V)	10 mm/s
Material Properties	Material	316L_NSWH
	Density (ρ)	7.966e-3 g/cm ³
	Emissivity (ϵ)	0.35
	Convective Heat Transfer Coefficient (h)	2e-5
	Temperature Range	1723.15 K, $T_0 = 293.15 \text{ K}$

Table 3.1. Process parameters and material Properties considered for the study

Tool path pattern considered for model training

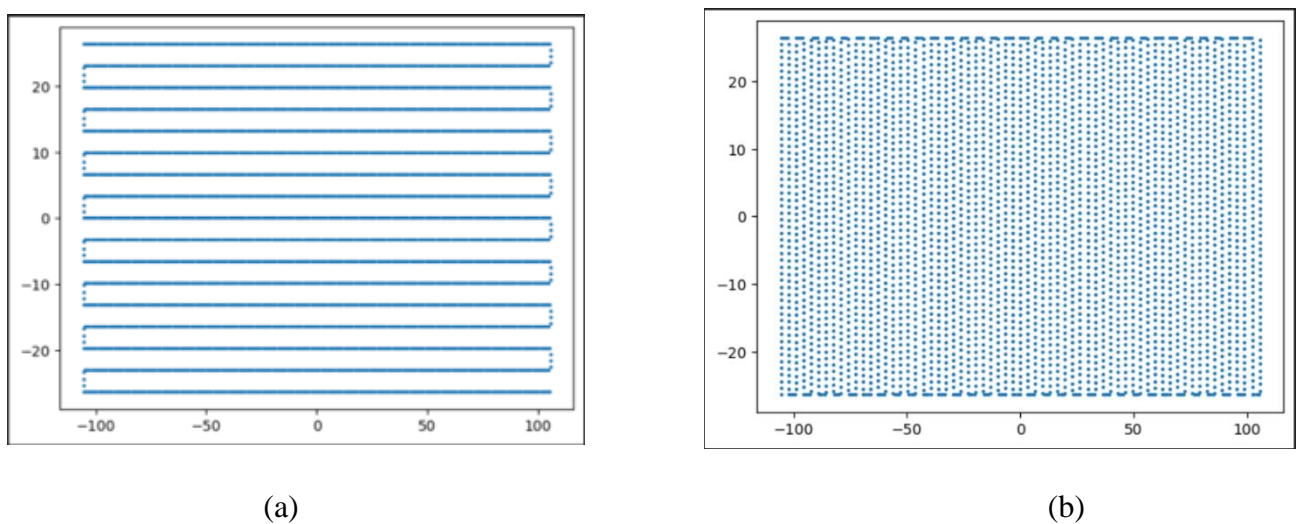


Fig 3.4. (a) Zigzag Horizontal pattern (b) Zigzag Vertical Pattern

3.2.2. Model Training:

After rigorous fine tuning of the model, the following model parameters are considered

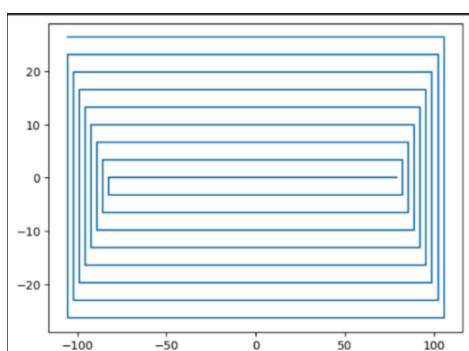
Category	Parameter	Value
Model Training	Patterns considered for training	Zigzag vertical and horizontal patterns
	Testing pattern	Contour In pattern
	Shape of neighbors	(7,7)
	Number of neighbors (num)	49
NN Related Parameters	Model architecture	[2*num, 6*num, 12*num, 6*num, 2*num, num]
	Learning rate and batch size	Lr= 0.0001 bs =128
	Loss term, optimizer	MSE loss, Adam

Table 3.2. Model training and NN parameters

3.2.3 Model evaluation:

3.2.3.1 Sequential Actual Temperature-Based Prediction

The model has been tested for predicting the temperature profile when the tool path follows a contour pattern. Temperatures generated using Simufact welding are considered as the actual temperatures. The model predicts the temperature at all points for time $t+2k$ prediction, using the actual temperatures from the previous step $t+k$ actual. We observed that the predicted temperatures closely match the actual temperatures measured using Simufact welding with 96.5 % accuracy score.



(a)

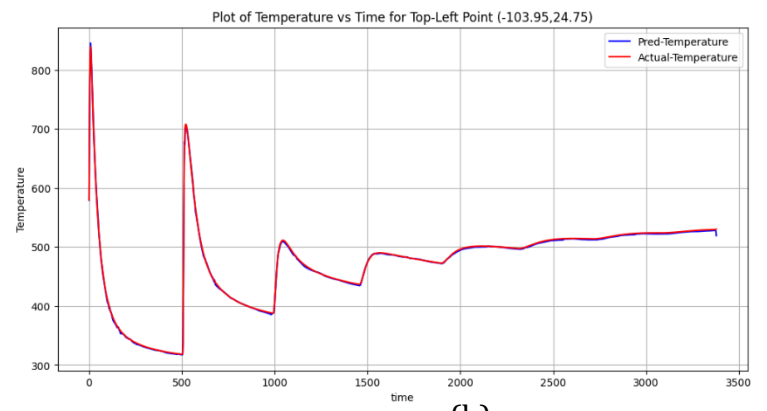


Fig 3.5. (a) Contour Pattern considered for testing (b) Comparison of Predicted and actual temperature at Top left corner point (-103.95, 24.75)

3.2.3.2 Sequential Iterative Prediction:

In this analysis, rather than using the actual temperature at the previous step ($t+k$)_{actual} to predict the temperature at ($t+2k$)_{prediction}, we use the predicted temperature at the previous step ($t+k$)_{prediction}. This iterative process continues, with each predicted temperature serving as the input for the next step, until the end of the thermal cycle.

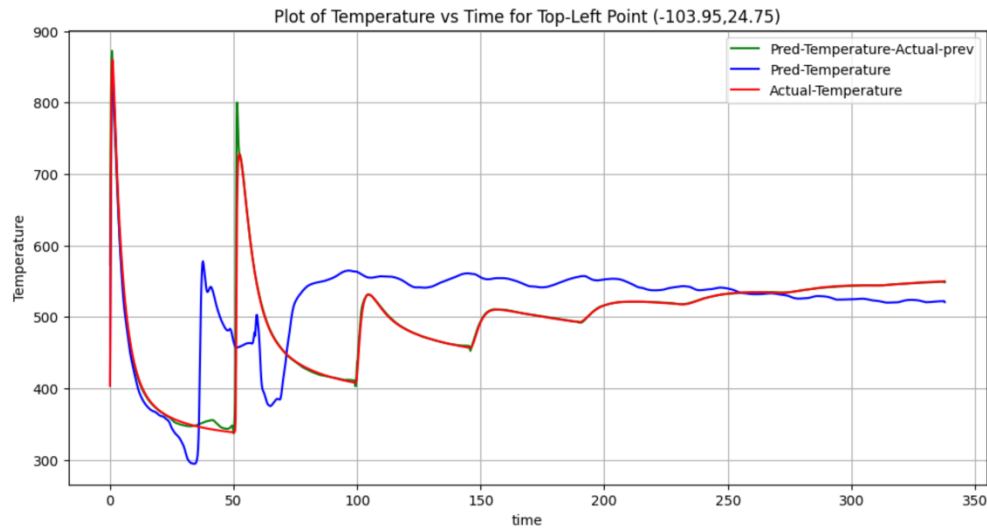


Fig 3.6. Time- temp Prediction at top left point (-103.95, 24.75)

The actual temperature (red curve) exhibits significant peaks at the beginning, which gradually stabilize over time. The model's predictions (blue and green curves) closely follow these initial peaks, indicating a good initial calibration of the model. The predicted temperatures (blue curve) closely match the actual temperatures (red curve) initially, but there is a noticeable divergence as time progresses. This divergence suggests that while the model can accurately predict short-term temperature changes, there may be factors causing discrepancies over longer periods. The green curve, which uses actual previous step temperatures as input, shows that incorporating actual measurements iteratively can enhance prediction accuracy. This method maintains closer alignment with the actual temperature profile compared to the blue curve, highlighting the importance of using accurate initial conditions in sequential predictions.

3.3 ML for AM: PINN approach

3.3.1 Governing Equations:

Think about a welding torch moving along the x-axis on a flat plate at a constant velocity v . The principle of energy balance (specifically enthalpy) is applied to a designated control volume. This principle dictates that the rate at which enthalpy increases within the control volume should be equal to the total of the rate at which heat flows into the control volume through its surfaces and the rate at which heat is generated within the control volume.

$$\Rightarrow \frac{d}{dt} \int_v H dv = - \int_s \vec{J} \cdot \vec{ds} + \int_v q dv \quad \text{----- Eq. 15}$$

Using the Fourier's law of heat conduction;

$$\vec{J} = -k \frac{\partial T}{\partial x} \quad \text{----- Eq. 16}$$

Using the divergence to convert surface integral into volume integral in above equation;

$$\begin{aligned} \Rightarrow \frac{d}{dt} \int_v H dv &= - \int_s (\vec{\nabla} \cdot \vec{J}) dv + \int_v q dv \\ \Rightarrow \frac{dH}{dt} &= \vec{\nabla} \cdot (k \vec{\nabla} T) + q \\ \Rightarrow \rho C_p \frac{dT}{dt} &= \vec{\nabla} \cdot (k \vec{\nabla} T) + q \quad \text{----- Eq. 17} \\ \Rightarrow \frac{dT}{dt} &= \frac{k}{\rho C_p} \nabla^2 T + \frac{q}{\rho C_p} \\ \Rightarrow \frac{\rho C_p}{k} \frac{dT}{dt} &= \nabla^2 T + q \end{aligned}$$

where H is enthalpy per unit volume, T is temperature, q is rate of heat generation, \vec{J} is heat flux, ρ is density of material, C_p is Specific heat at constant pressure and α is reciprocal of thermal diffusivity.

Since, we are Considering the heat source is applied as a surface flux, the $q = 0$, since no internal heat generation is present in our study.

3.3.2 Assumptions considered for the Study:

- The latent heat of phase change was neglected in the material properties because it had minimal impact on the temperature distribution (this study only considers a single phase).
- The internal flow of the melt pool during deposition and heat loss from evaporation were also ignored. Initial temperature is considered as room temperature.
- Bottom surface of the plate is kept as insulated surface.

In heat equation, temperature T is function of spatial coordinates (x, y, z) and time t.

3.3.3 Boundary conditions

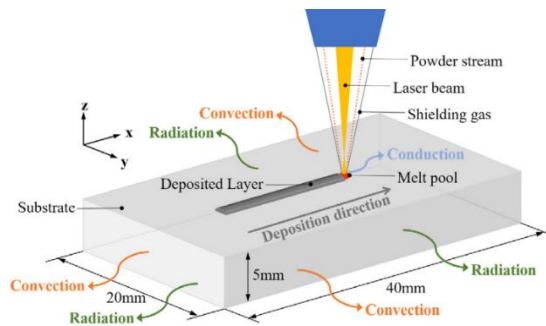


Fig: 3.7 Schematic of Process physics with Boundary condition of Metal Additive process [15]

The heat source flux is assumed to be applied only to the top surface, while the convective and radiative heat fluxes are applied to all surfaces. These can be expressed as:

$$\begin{aligned} -k\vec{\nabla}T \cdot n &= q_{heat\ source} + q_{rad} + q_{conv} \\ q_c &= h_c(T - T_a) \\ q_r &= \sigma\epsilon(T^4 - T_a^4) \end{aligned} \quad : ----- \text{ Eq. 18}$$

$n = [n_x, n_y, n_z]$, Unit normal vector on the surface

For the bottom surface of the substrate, where a Dirichlet boundary condition is applied:

$$T_{z=0} = T_0$$

3.3.4 Implementation of PINN model without Auxiliary data:

3.3.4.1 Example problem on Laser material processing:

Dynamic heat conduction in bulk materials can be modelled by the time-dependent heat conduction equation, which is a partial differential equation in both space \vec{x} and time t:

$$c_p \frac{\partial}{\partial t} u(\vec{x}, t) = \frac{\kappa}{\rho} \Delta u(\vec{x}, t) + \dot{Q}(\vec{x}, t) \quad \text{----- Eq. 19}$$

For the heat source, a Gaussian beam profile was used with a laser power $P_L=1$ W and a velocity of 1 mm/s. The heat source is modelled by:

$$\dot{Q} = \frac{2 \cdot P_L}{\pi \cdot r_{\text{spot}}^3} \cdot \exp\left(-2 \cdot \frac{r_{\text{focus}}^2}{r_{\text{spot}}^2}\right) \quad \text{----- Eq. 20}$$

The temperature field is modeled within a finite cube. A Dirichlet boundary condition (BC) was applied to its lower base and set to 0.

For the four lateral faces (F) the Neumann BC was

$$\frac{\partial}{\partial t} u(\vec{x}, t) = 0.1 \quad \text{----- Eq. 21}$$

The initial conditions (IC) were set to $u = 0$ for the entire domain. These conditions are motivated by the typical setup in Laser-DED.

Implementation details:

The IC and BCs for the simulation were set as follows: a Dirichlet boundary condition was applied at the lower base, fixing the temperature u to 0, while a Neumann boundary condition was imposed on the lateral faces as expressed as Eq. 21

The initial temperature throughout the domain was set to 0. The laser settings included a laser power of 1 W and velocity components ($v_x = 1$), ($v_y = 0$), and ($v_z = 0$)

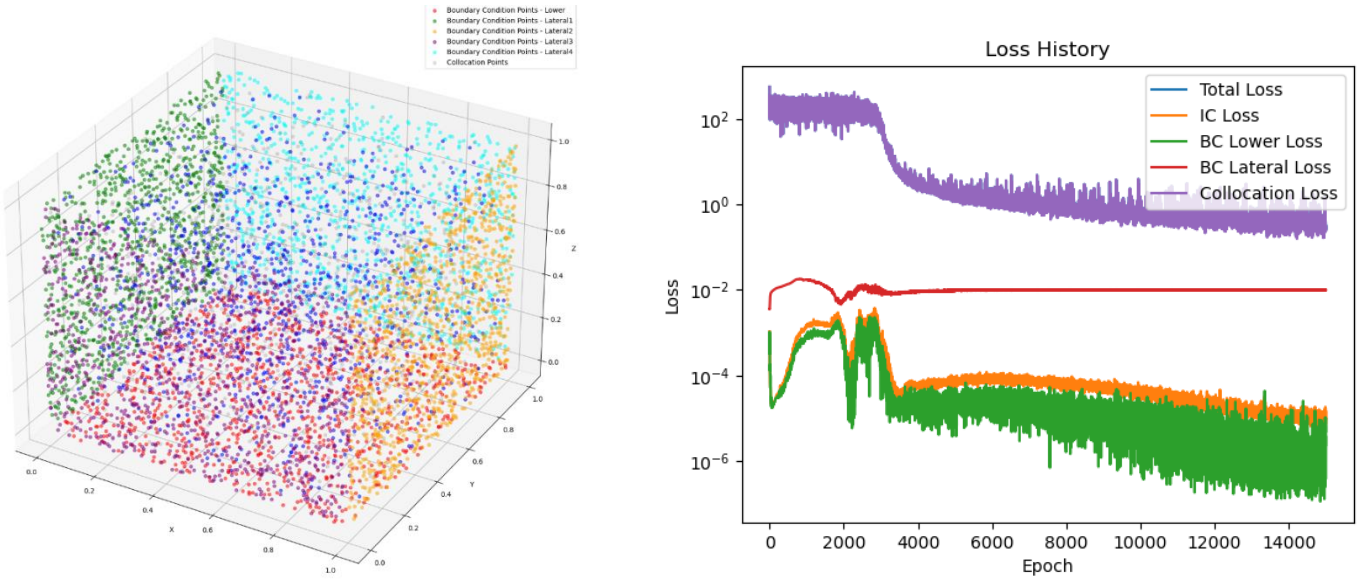


Fig: 3.8 (a) 3D Latin hypercube sampling of Domain (b) Loss curves

For the training process, Latin Hypercube sampling strategy is used to generate 1000 points were sampling for the initial condition, 1000 points for the boundary conditions, and 8000 collocation points were generated. The optimization of the neural network was performed using the Adam optimizer with a learning rate of 0.001 over a total of 15,000 epochs. The neural network architecture comprised an input layer with 4 nodes (t, x, y, z), four hidden layers each with 50 nodes, and an output layer with a single node representing temperature. The Tanh activation function was employed throughout the network. The model took only 14 min to train and it has been observed that results are exactly matching with the research article taken as a reference for this implementation.

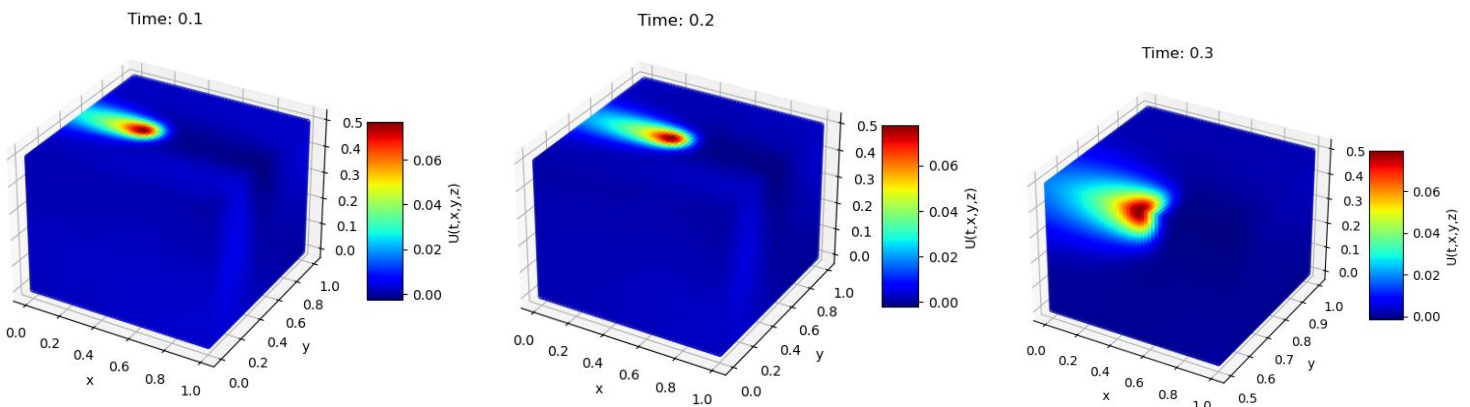


Fig: 3.9 Model predictions at $t = 0.1, 0.2$ and 0.3 sec

3.3.4.2 3D temperature field without auxiliary data in process of laser DED

The problem is modeled using a partial differential equation (PDE) that describes heat conduction and includes boundary conditions for convection and radiation.

1. Governing equations:

The governing equation of transient heat conduction in additive manufacturing (AM) can be written as:

$$\rho C_p \frac{\partial T}{\partial t} + \nabla \cdot q = 0 \quad \text{----- Eq. 22}$$

where:

- ρ is the density of the material (g/mm^3).
- C_p is the heat capacity (J/gK).
- T is the temperature (K).
- t is the time (s).

According to Fourier's law of heat conduction, the heat flux q is given by:

$$q = -k\nabla T \quad (\text{W/mm}^2) \quad \text{----- Eq. 23}$$

where k is the thermal conductivity in W/mmK .

The heat flux of the laser q_{laser} is defined as:

$$q_{\text{laser}} = \frac{2P\eta}{\pi r^2} \exp \left(-2 \frac{(x-x_0-vt)^2+(y-y_0)^2}{r^2} \right) \cdot (t \leq t_{\text{end}}) \cdot (t > 0) \quad \text{----- Eq. 24}$$

where:

- η is the laser absorptivity.
- P is the laser power (W).
- r is the radius of the laser beam (mm).
- x_0 and y_0 are the initial coordinates of the laser spot.
- v is the velocity of the laser movement.
- t is the time.

The governing equation for the problem turns out into:

$$\rho C_p \frac{\partial T}{\partial t} = k \left(\frac{\partial^2 T}{\partial x^2} + \frac{\partial^2 T}{\partial y^2} + \frac{\partial^2 T}{\partial z^2} \right) \quad \text{----- Eq. 25}$$

2. Boundary Condition Implementation

The heat source flux is assumed to be applied only to the top surface, while the convective and radiative heat flux is applied to all surfaces. These can be expressed as:

The boundary conditions for the problem are given by:

- For the surfaces at $x = \pm x, y = \pm y$:

$$k \frac{\partial T}{\partial n} = q_{\text{rad}} + q_{\text{conv}}$$

- For the surfaces at $z = \pm z$:

-

$$T_t = 0 \text{ (bottom surface)} \\ k \frac{\partial T}{\partial z} = q_{\text{laser}} + q_{\text{rad}} + q_{\text{conv}} \quad \text{----- Eq. 26}$$

where:

- $q_{\text{conv}} = h_c(T - T_a)$
- $q_{\text{rad}} = \sigma\epsilon(T^4 - T_a^4)$ ----- Eq. 27

3. Custom Point discretisation strategy of domain followed:

- The domain, measuring 40x10x6 mm, was point wise distributed at 1 mm intervals with a time step of 0.05 seconds
- The top layer (40x10 mm up to 1 mm depth) was point wise distributed at a finer interval of 0.5 mm due to higher thermal gradients.
- Near toolpath origin also, more points were sampled with mesh grid of 4*4 mm with 0.5 mm intervals for ease of capturing the temperature of

surrounding particles from initial state, when heat source is just about to start from its origin

- To effectively model the heat source dynamics in Metal AM, a finer mesh grid of 6x6 mm with 0.25 mm intervals was used near the source area.

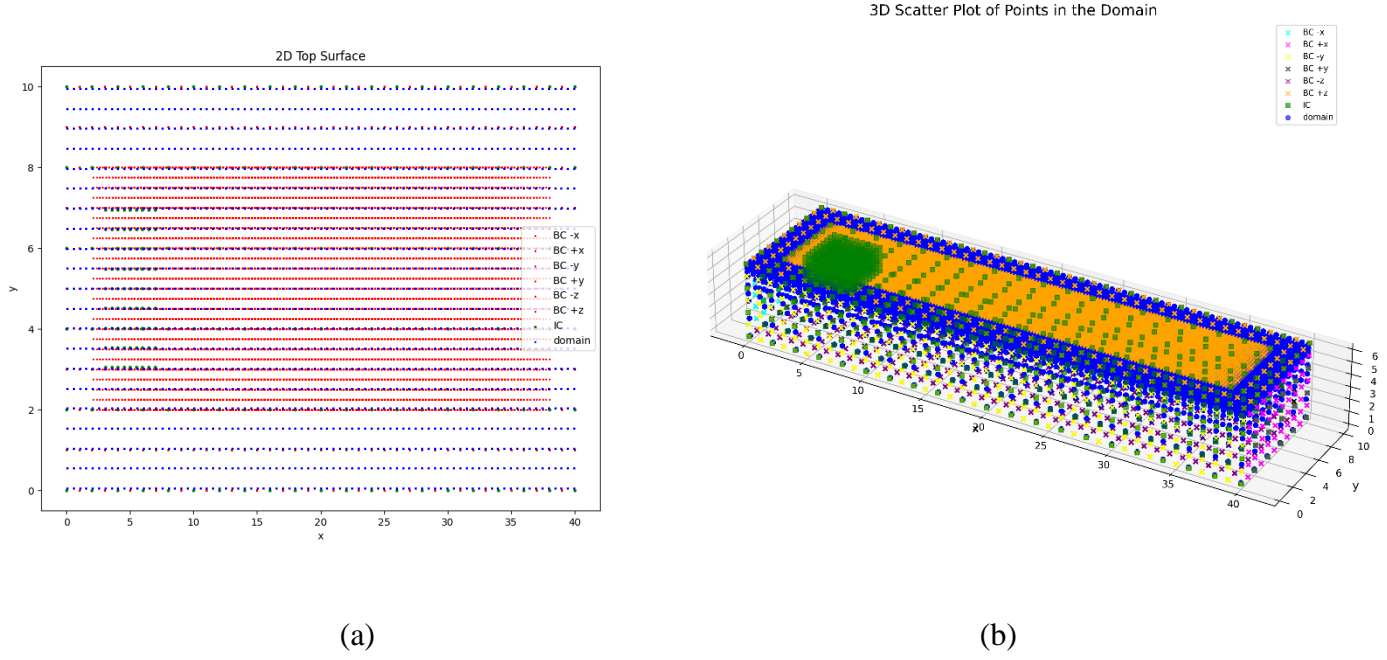


Fig 3.10: (a) 2D Top surface sampling (b) 3D custom sampling strategy of domain

Process and Material Properties:

Parameters	Values
Laser Parameters	
Laser Power (P)	500 W
Radius of Laser (r)	1.5 mm
Laser Absorptivity (η)	0.4
Laser Speed (V)	10 mm/s
Material Properties	
Specific Heat Capacity (Cp)	0.5 J/gK
Thermal Conductivity (K)	0.01 W/mmK
Emissivity (ϵ)	0.3
Maximum Temperature Range	3000 K
Density	8e-3 g/mm ³

Table 3.3 Process parameters and Material properties

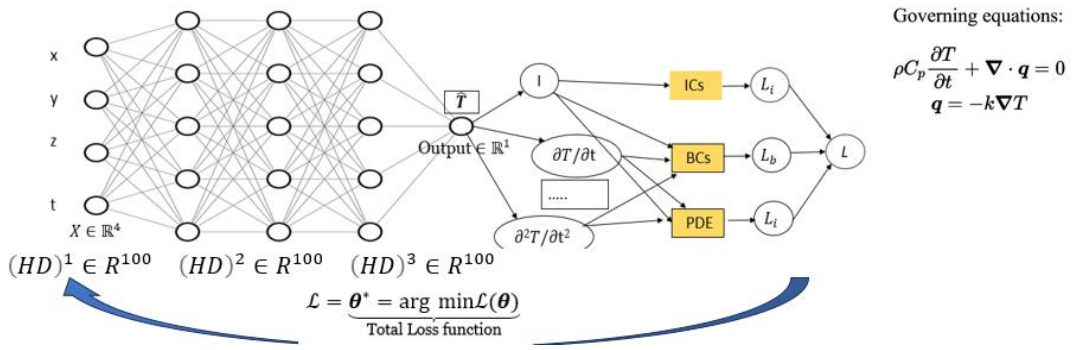


Fig 3.11. PINN Architecture Followed

A 3-dimensional transient heat transfer analysis subjected to boundary and initial conditions as discussed above have been implemented in the PINN model using custom sampling strategy as discussed earlier.

The input layers take the space and time coordinates. The architecture consists of 3 hidden layers each $\epsilon \mathbb{R}^{100}$ and the output layer $\epsilon \mathbb{R}^1$ predicts the temperature variable. Automatic differentiation technique is used to form the required components of PDE, and a combined loss function is constructed which is a weighted sum of all the different losses (BC Loss, IC Loss, PDE Loss) as shown below.

Network and training parameters:

Parameter	Value
Layer Architecture	[4, 100, 100, 100, 1]
Activation function	Linear, Tanh for Hidden layers, Softplus for output
Epochs	50000
Learning rate	2e-4
Input Transform	Normalization between [-1, 1]

Table 3.4. PINN Network Parameters for L-DED

Loss Functions:

$$\begin{aligned}
 \text{Boundary Loss : } \quad \mathcal{L}_b &= \frac{1}{N_b} \sum_{k=1}^{N_b} |\mathcal{B}(\hat{T}(\mathbf{x}_b^k, t_b^k), \mathbf{x}_b^k, t_b^k)|^2, \\
 \text{Initial Loss: } \quad \mathcal{L}_i &= \frac{1}{N_i} \sum_{k=1}^{N_i} |\hat{T}(\mathbf{x}_i^k, 0) - I(\mathbf{x}_i^k)|^2, \quad \text{----- Eq. 28} \\
 \text{PDE Loss : } \quad \mathcal{L}_r &= \frac{1}{N_r} \sum_{k=1}^{N_r} |\hat{T}(\mathbf{x}_r^k, t_r^k) - \mathcal{N}[\hat{T}]|^2,
 \end{aligned}$$

where N_b , N_i , and N_r are the number of sampling points for each loss term.

Combined Loss:

$$L = w_b L_b + w_i L_i + w_r L_r \quad \text{----- Eq. 29}$$

Where w_b , w_i , w_r are the weights considered as each loss in order to adjust the importance on the which loss to be optimized as per the training situation. The weights considered for this study are [2.0, 1.0, 1.0, 1.0]. After hyper parameter tuning and architectural changes, it has been found that a learning rate of 2e-4 and architecture of [4, 100, 100, 100, 1] with 50000 epochs found to be converged as shown in the loss curve. The training took 1.3 hr approx. on a RTX 2080 Ti GPU

4. Model evaluation:

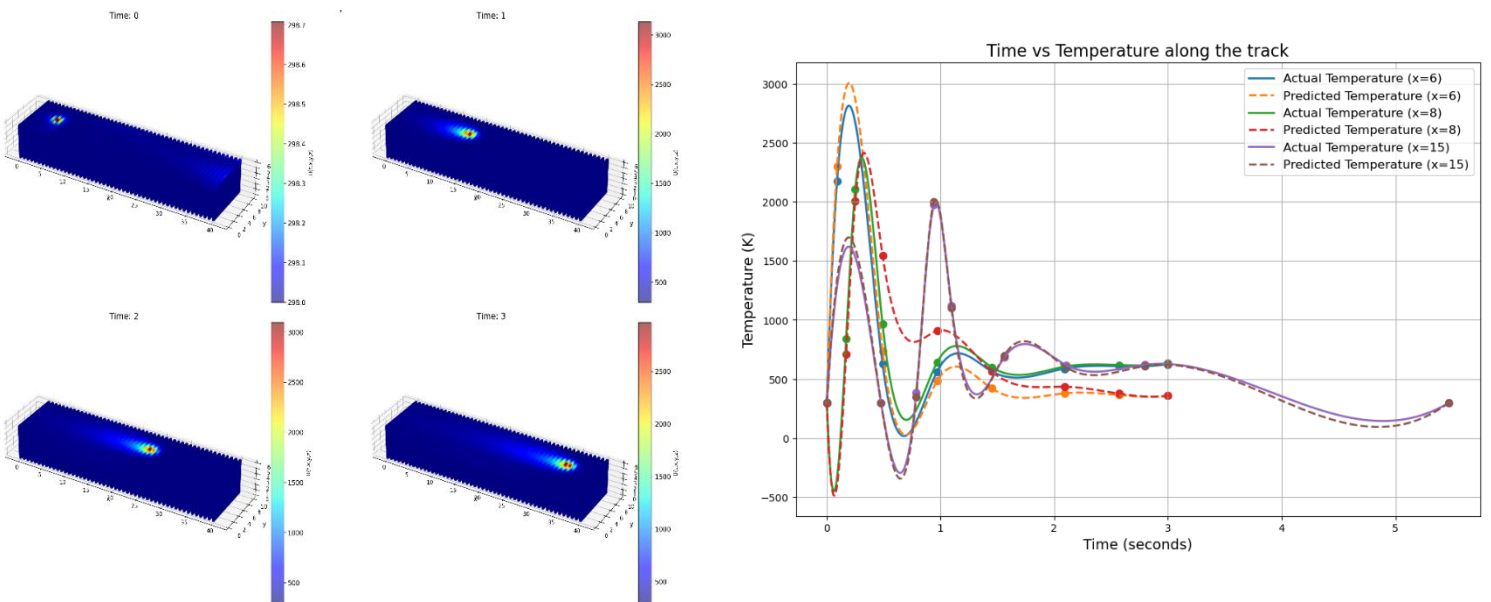
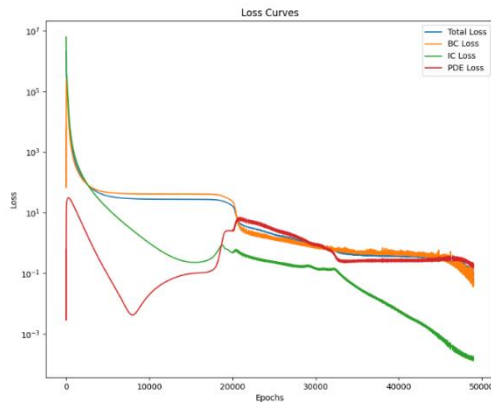
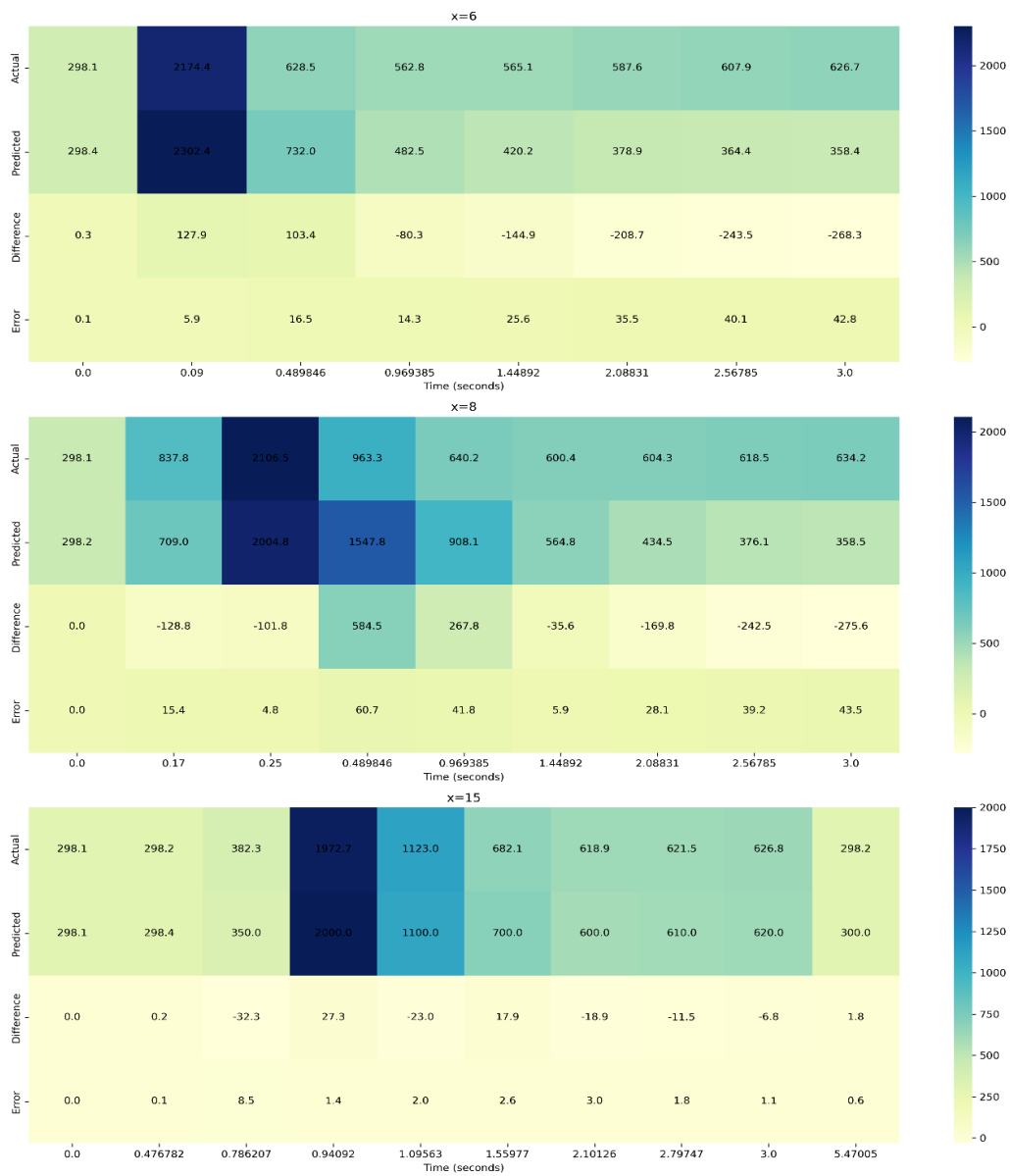


Fig 3.12 (a) 3D model Predictions at $t= 0, 1, 2, 3$ sec (b) Comparison analysis of model predictions with simulation results



(a)

Actual vs Predicted Temperatures with Differences and Percentage Errors



(b)

Fig 3.13. (a) Loss curves (b) Error analysis

In this study, we evaluated the predictive accuracy of our model by comparing actual and predicted temperature values at multiple positions along the track. We computed temperature differences and percentage errors for each position and visualized these comparisons using heatmaps.

To provide a comprehensive measure of the model's accuracy, we calculated the average percentage error across the entire domain. The resulting average percentage error was found to be 16.34%, indicating the overall prediction accuracy of the model. This value provides a benchmark for assessing and improving the model's performance.

3.3.4.3 3D temperature field prediction without auxiliary data for process of WAAM

Wire Arc Additive Manufacturing (WAAM), developed from Gas Metal Arc Welding (GMAW), Gas Tungsten Arc Welding (GTAW), or Plasma Arc Welding (PAW), is considered the most suitable candidate for fabricating large-scale metallic structures due to its high deposition rates and low feedstock and equipment costs.

In this section we will carry out a 3D transient thermal analysis on GMAW based Wire arc additive Manufacturing using PINN model.

The Boundary and Initial conditions for the process remains same as that of laser DED seen earlier. The major change comes with the heat source, where in WAAM we majorly use Goldak double ellipsoidal heat source as shown below.

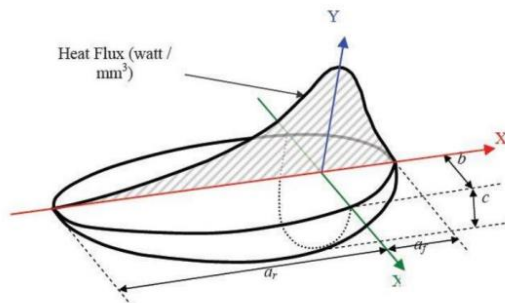


Fig 3.14. Goldak Double Ellipsoidal Heat Source [16]

1. Governing equations:

The Governing equations and boundary conditions discussed previously are pretty much valid here as well, the major change comes with the volumetric double ellipsoidal Goldak heat source. Since the Goldak heat source is a volumetric heat source and acts as an body flux. The heat source should be incorporated in PDE Residual instead as BC on Top surface as in case of Laser-DED.

So, the PDE will be converted as

$$\rho C_p \frac{\partial T}{\partial t} = k \left(\frac{\partial^2 T}{\partial x^2} + \frac{\partial^2 T}{\partial y^2} + \frac{\partial^2 T}{\partial z^2} \right) + q_{\text{source/arc}}$$

$$q_{\text{arc}} = \begin{cases} \frac{6\sqrt{3}f_f\eta UI}{a_f b c \pi \sqrt{\pi}} \exp\left(-3\left(\frac{(x-x_0-V_T t)^2}{a_f^2} + \frac{(y-y_0)^2}{b^2} + \frac{(z-z_0)^2}{c^2}\right)\right) & ((x-x_0-V_T t) > 0) \\ \frac{6\sqrt{3}f_r\eta UI}{a_r b c \pi \sqrt{\pi}} \exp\left(-3\left(\frac{(x-x_0-V_T t)^2}{a_r^2} + \frac{(y-y_0)^2}{b^2} + \frac{(z-z_0)^2}{c^2}\right)\right) & ((x-x_0-V_T t) < 0) \end{cases} \quad \text{---- Eq. 30}$$

Parameter	Value (mm)
Front semi-axis length (a_f)	1.002
Rear semi-axis length (a_r)	3.34
Half width of arc (b)	1.67
Depth of arc (c)	1.67
Gaussian distribution	3

Table 3.5. Goldak Double ellipsoidal Heat source parameters

2. Custom Point discretisation strategy of domain followed:

- The domain, measuring from the specified minimum to maximum bounds, was point-wise distributed at varying intervals with a time step of approximately 0.05 seconds.
- The main domain was point-wise distributed at 2 mm intervals.
- The top layer (up to 3 mm depth) was point-wise distributed at a finer interval of 1 mm and even finer at 0.5 mm near the top surface due to higher thermal gradients.

- Near the toolpath origin, more points were sampled with a mesh grid of 4x4 mm using 0.5 mm intervals for ease of capturing the temperature of surrounding particles from the initial state when the heat source is just about to start from its origin.
- To effectively model the heat source dynamics, a finer mesh grid of 6x6 mm with 0.25 mm intervals was used near the source area.

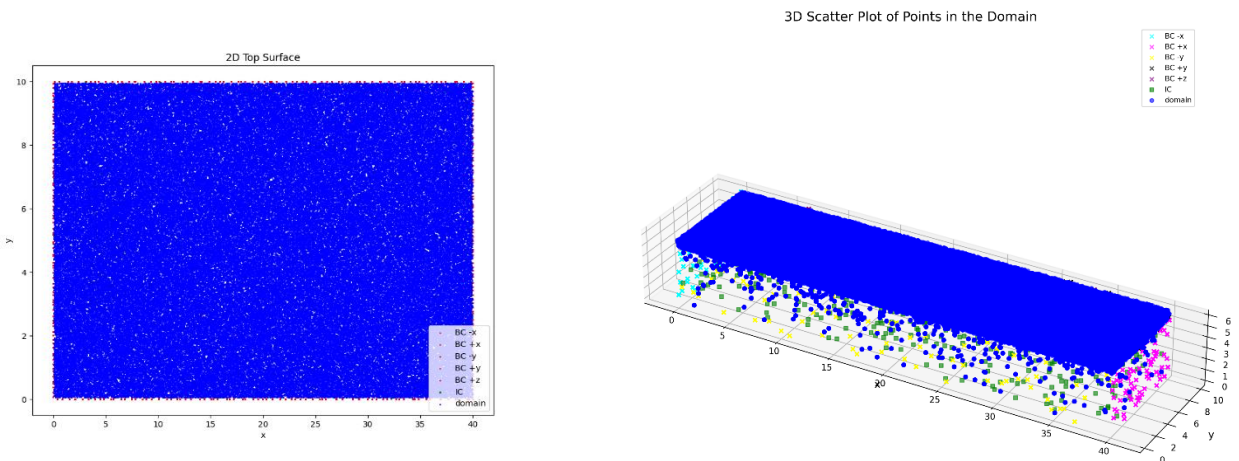


Fig 3.15. (a) 2D Top surface sampling (b) 3D domain and Boundary sampling

Process parameters and material properties:

Parameters	Values
Process Parameters	
Velocity (v) mm/s	10.0
Voltage (U) Volts	15.3
Current (I) Watt	120
Efficiency (η)	0.9
Convective Coefficient (h) W/mm ² K	2e-5
Emissivity (ϵ)	0.3
Stefan-Boltzmann Constant (Rboltz) W/mm ² K ⁴	5.6704e-14
Reference Temperature (T_ref) and Temperature range Kelvin	T_ref= 298.15 K, T_range= 4800 K
Material Properties	
Specific Heat (Cp) J/gK	0.6
Thermal Conductivity (k) W/mmK	0.024

Density g/mm ³	7.966e-3
Neural Network Parameters	
Iterations and learning rate	30000, lr= 2e-4
Architecture	[4, 64, 64, 64, 1]

Table 3.6. Process, material and Model parameters for WAAM

Combined Loss:

$$L = w_b L_b + w_i L_i + w_r L_r \quad \text{----- Eq. 29}$$

Where w_b , w_i , w_r are the weights considered as each loss in order to adjust the importance on the which loss to be optimized as per the training situation. The weights considered for this study are [1e-2, 1e-2, 1.5] After hyper parameter tuning and architectural changes, it has been found that a learning rate of 2e-4 and architecture of [4, 64, 64, 64, 1] with 50000 epochs found to be converged as shown in the loss curve. The training took 1.1 hr approx. on a RTX 2080 Ti GPU.

Model evaluation:

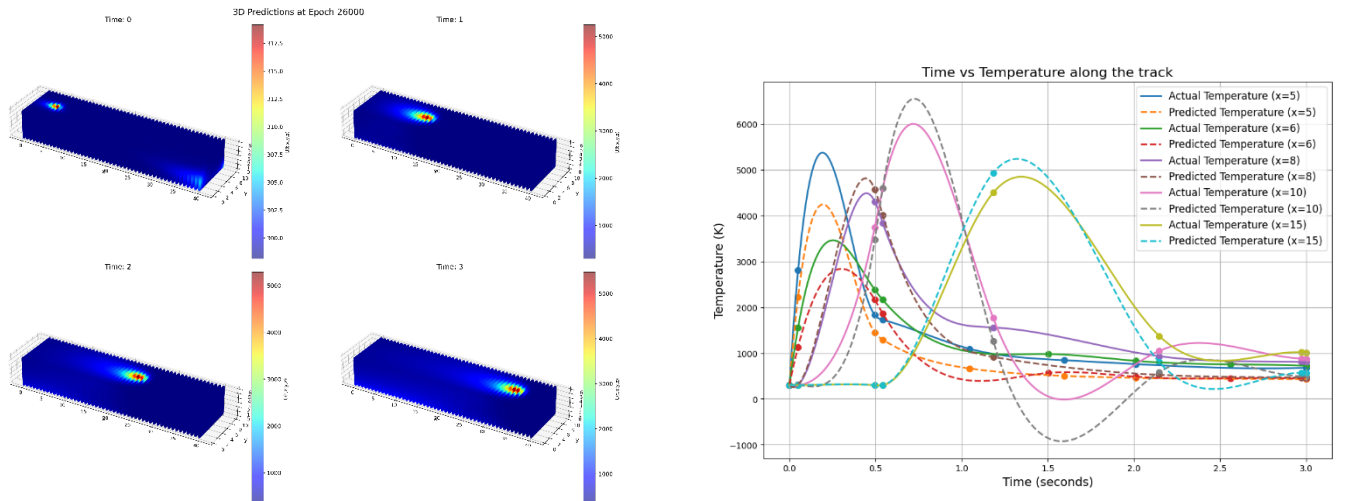
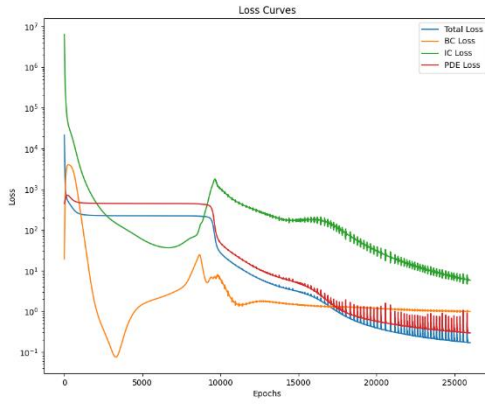
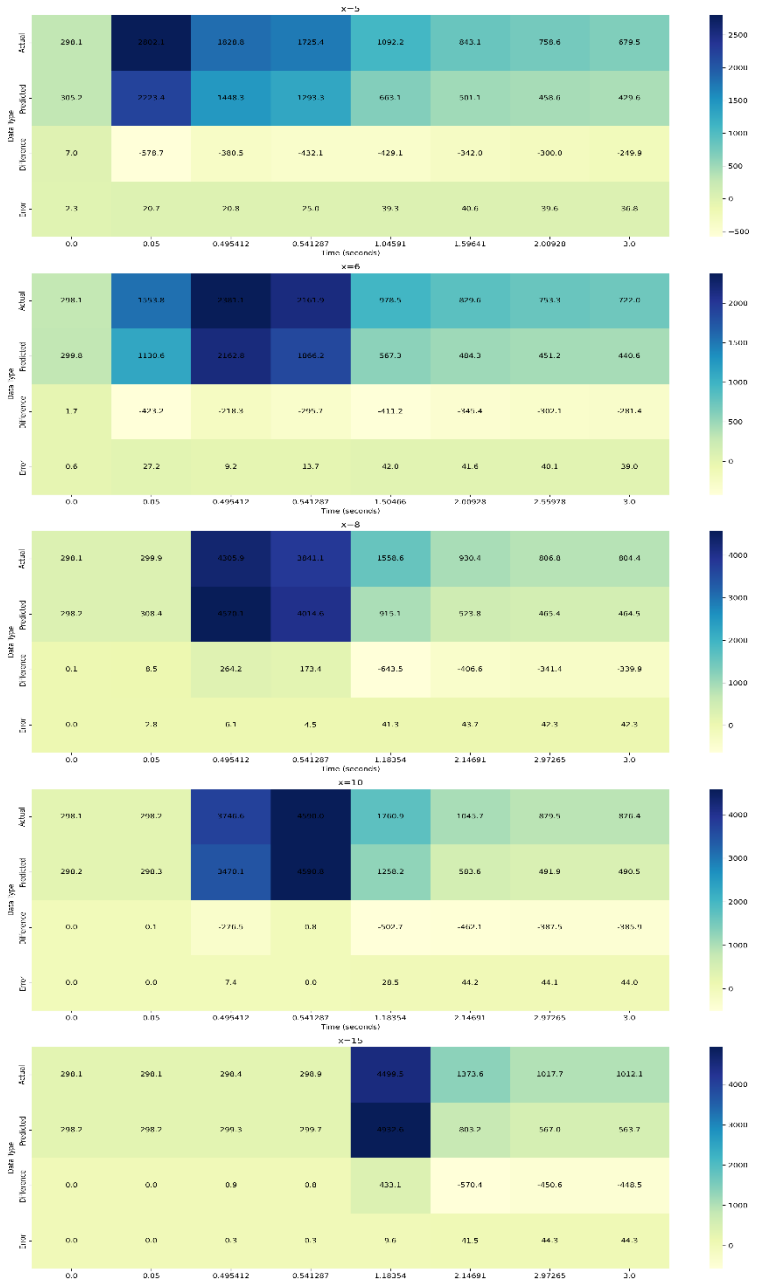


Fig 3.16 (a) 3D model Predictions at t= 0, 1, 2, 3 sec (b) Comparison analysis of model predictions with simulation results



(a)

Actual vs Predicted Temperatures with Differences and Percentage Errors



(b)

Fig 3.17. (a) Loss curves (b) Error analysis

In this study, we evaluated the predictive accuracy of our model by comparing actual and predicted temperature values at multiple positions along the track. We computed temperature differences and percentage errors for each position and visualized these comparisons using heatmaps.

To provide a comprehensive measure of the model's accuracy, we calculated the average percentage error across the entire domain. The resulting average percentage error was found to be 23.25%, indicating the overall prediction accuracy of the model. This value provides a benchmark for assessing and improving the model's performance.

3.3.4.4 3D Transient Thermal analysis on WAAM considering Temperature dependent properties

In this analysis Temperature dependent properties are considered maintaining all other NN and process parameters constant of constant material properties case

$$k = (0.01351T + 10.03816)/1000 \quad \text{W/mmK}$$

$$C_p = (0.16242T + 433.30551)/1000 \quad \text{J/gK} \quad \text{----- Eq. 30}$$

1. Model Evaluation:

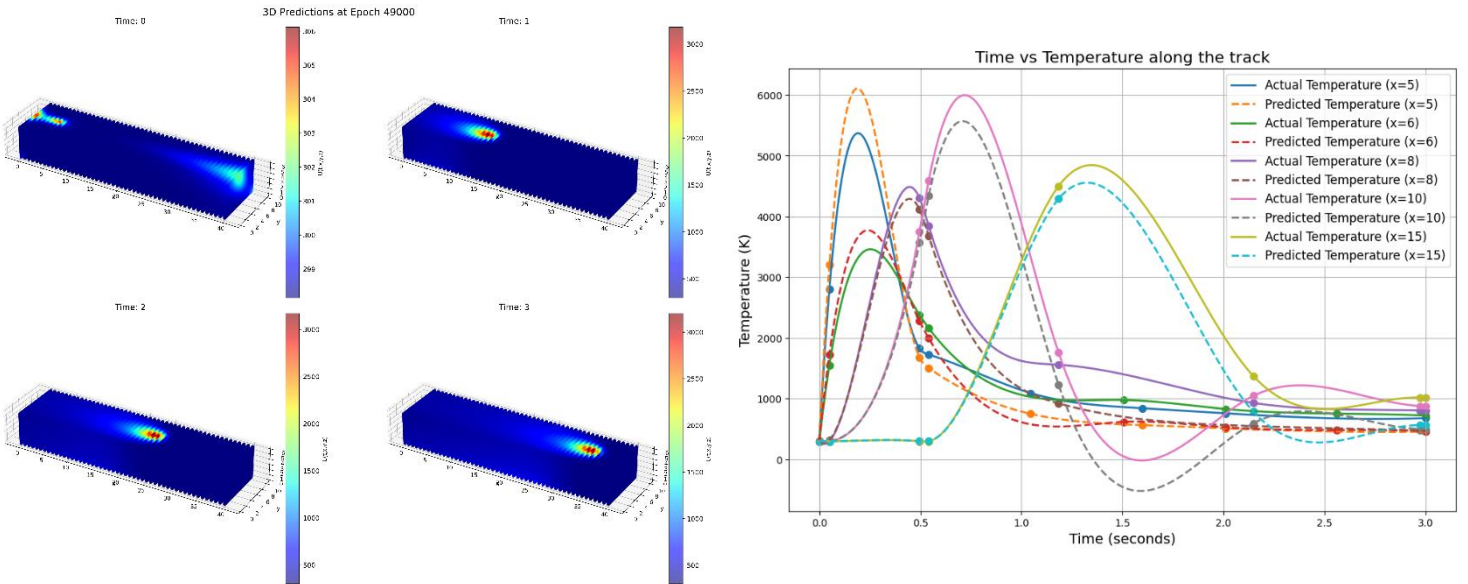
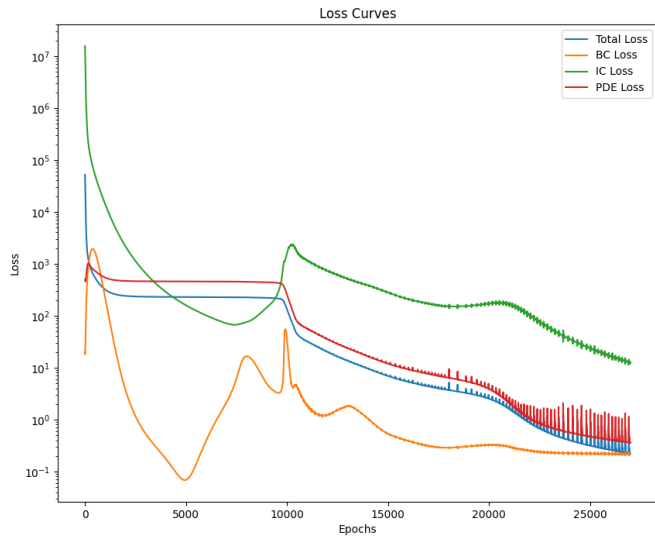
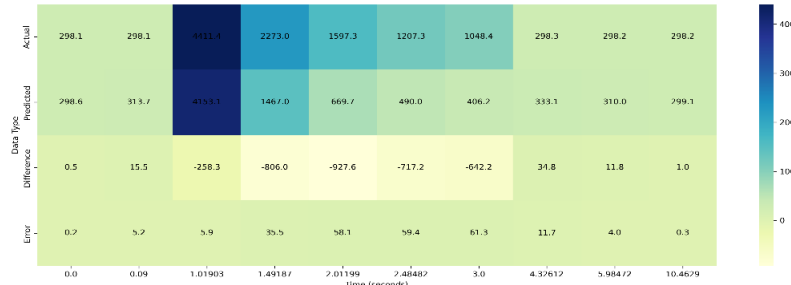
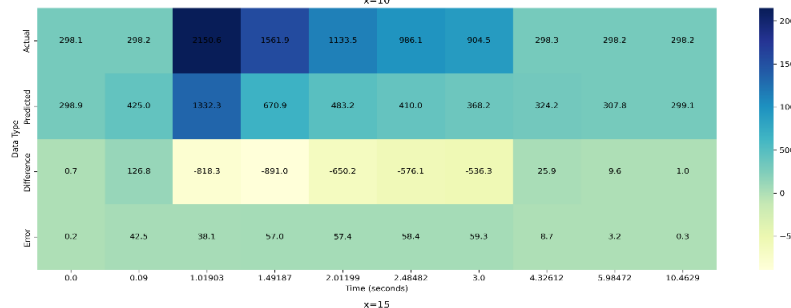
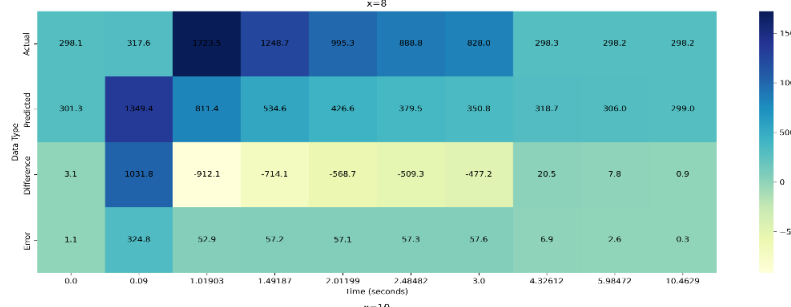
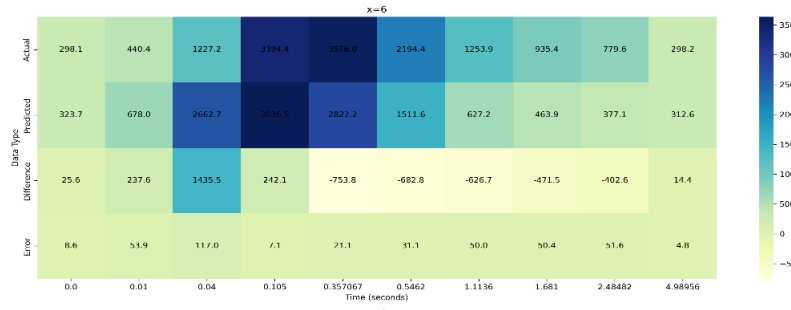


Fig 3.18 (a) 3D model Predictions at t= 0, 1, 2, 3 sec (b) Comparison analysis of model predictions with simulation results



(a)

Actual vs Predicted Temperatures with Differences and Percentage Errors



(b)

Fig 3.19. (a) Loss curves (b) Error analysis

In this case, we evaluated the predictive accuracy of our model by incorporating the Temperature dependent properties by comparing actual and predicted temperature values at multiple positions along the track. We computed temperature differences and percentage errors for each position and visualized these comparisons using heatmaps.

To provide a comprehensive measure of the model's accuracy, we calculated the average percentage error across the entire domain. The resulting average percentage error was found to be 20.56%, indicating the overall prediction accuracy of the model. This value provides a benchmark for assessing and improving the model's performance.

3.3.4.5 Hybrid PINN model (With auxiliary data) for modelling of WAAM process:

In this approach we include data component to the loss function to improve the PINN performance. The input layers takes the space and time coordinates, The architecture consists of 3 hidden layers each $\epsilon \mathbb{R}^{64}$ and the output layer $\epsilon \mathbb{R}^1$ predicts the temperature variable. Automatic differentiation technique is used to form the required components of PDE, and a combined loss function is constructed which is a weighted sum of all the different losses (BC Loss, IC Loss, PDE Loss, Data loss (in case of Hybrid model)) as shown below.

- Randomly sampled 174 data points are considered as a partial data to support the loss function for better optimization. Training of this model took around 2.1 hr on RTX 2080 Ti GPU.

Loss Functions:

$$\begin{aligned}
 \text{Boundary Loss : } \quad \mathcal{L}_b &= \frac{1}{N_b} \sum_{k=1}^{N_b} \left| \mathcal{B}(\hat{T}(\mathbf{x}_b^k, t_b^k), \mathbf{x}_b^k, t_b^k) \right|^2, \\
 \text{Initial Loss: } \quad \mathcal{L}_i &= \frac{1}{N_i} \sum_{k=1}^{N_i} \left| \hat{T}(\mathbf{x}_i^k, 0) - I(\mathbf{x}_i^k) \right|^2, \\
 \text{PDE Loss : } \quad \mathcal{L}_r &= \frac{1}{N_r} \sum_{k=1}^{N_r} \left| \hat{T}(\mathbf{x}_r^k, t_r^k) - \mathcal{N}[\hat{T}] \right|^2,
 \end{aligned}$$

$$\text{Data Loss (In case of hybrid model): } \quad \mathcal{L}_d = \frac{1}{N_d} \sum_{k=1}^{N_d} |\hat{T}(x_r^k, t_r^k) - T(x_r^k, t_r^k)|^2$$

where N_b, N_i , and N_r, N_d are the number of sampling points for each loss term

Combined Loss:

$$L = w_b L_b + w_i L_i + w_r L_r + w_d L_d$$

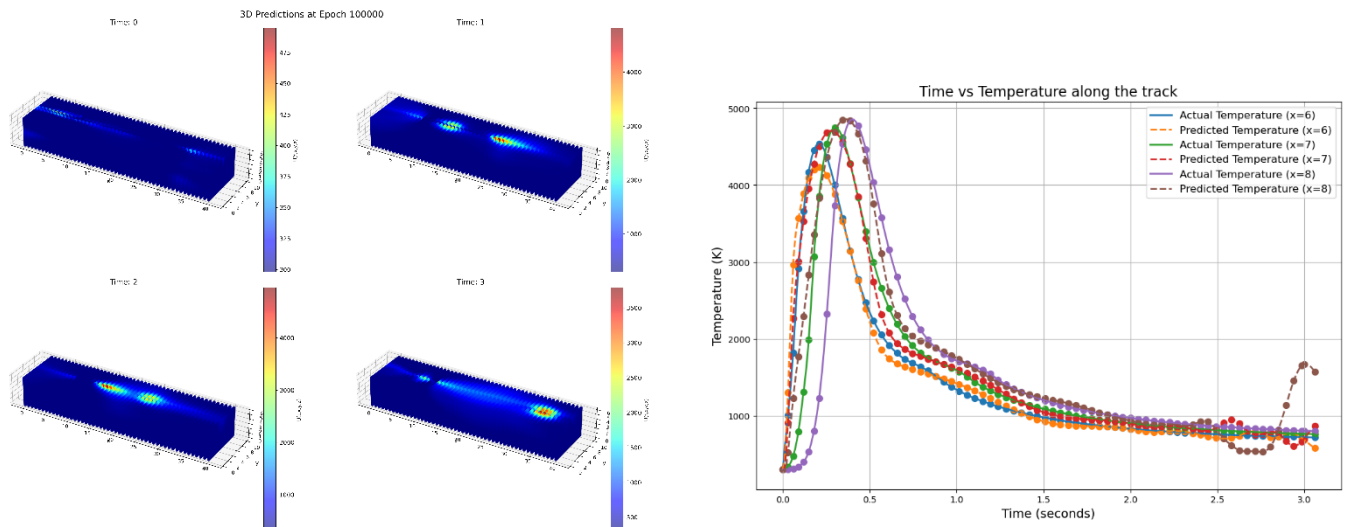
Where w_b, w_i, w_r, w_d are the weights considered as each loss in order to adjust the importance on the which loss to be optimized as per the training situation. The weights considered for the study are [1, 1e-1, 1, 3.0]

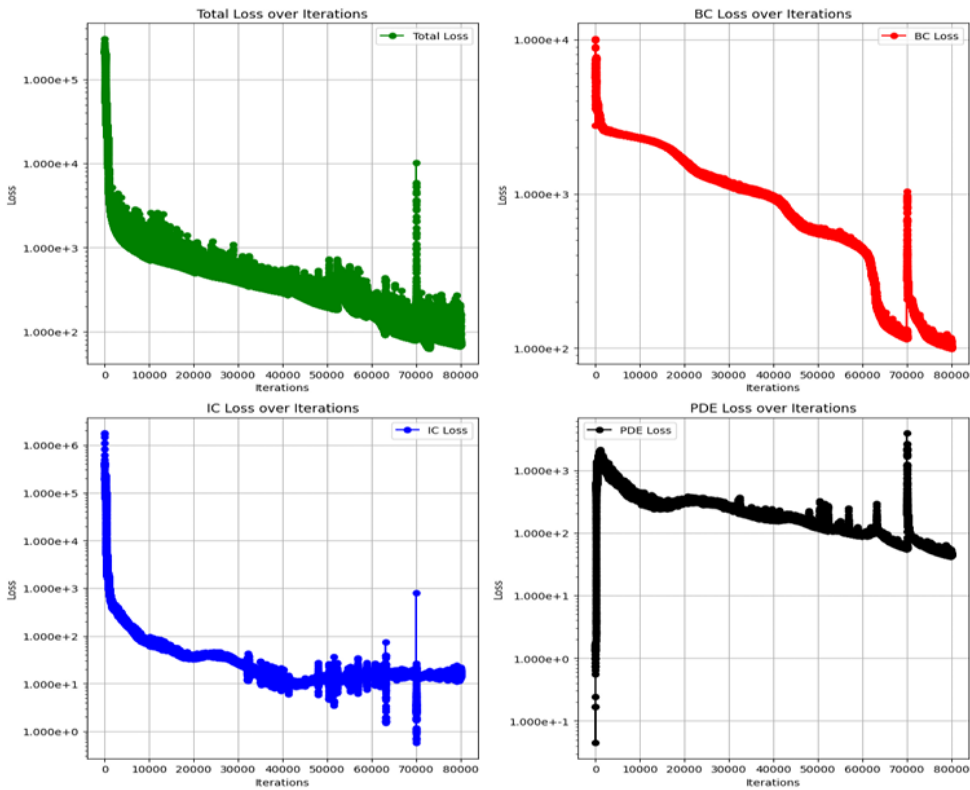
Model parameters:

Parameter	Value
Iterations	80000
Learning rate	2e-3
Architecture	[4, 64, 64, 64, 1]
Number of BC points (N_{bc})	215854
Number of IC points (N_{ic})	1219
Number of domain points	416874
Number of data points (N_d)	174
Total number of points	634121

Table 3.7. Hybrid Model parameters for WAAM

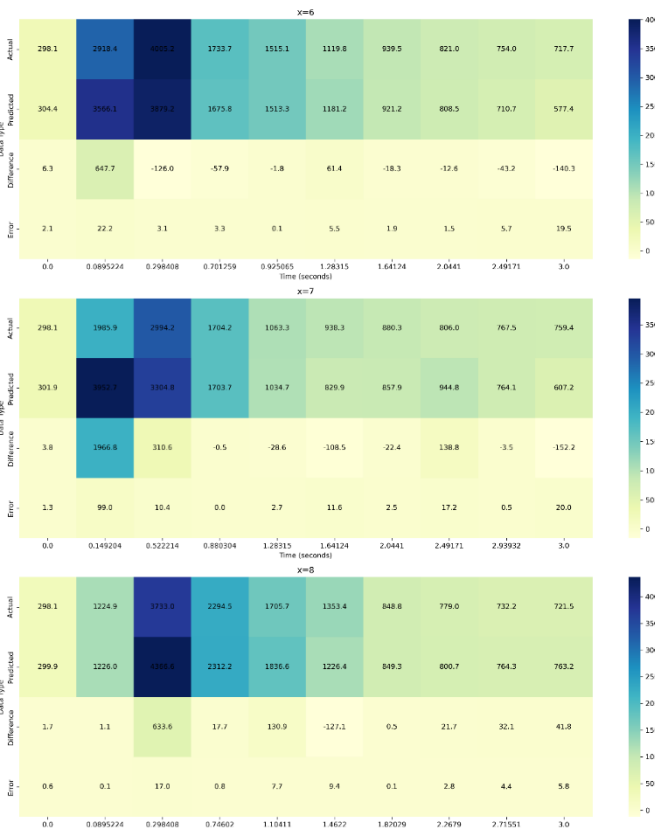
1. Model evaluation:





(a)

Actual vs Predicted Temperatures with Differences and Percentage Errors



45 (b)

Fig 3.21. (a) Loss curves (b) Error analysis

In this Hybrid model, we evaluated the predictive accuracy of our model by comparing actual and predicted temperature values at multiple positions along the track. We computed temperature differences and percentage errors for each position and visualized these comparisons using heatmaps.

To provide a comprehensive measure of the model's accuracy, we calculated the average percentage error across the entire domain. The resulting average percentage error was found to be 9.3%, indicating the overall prediction accuracy of the model. This value provides a benchmark for assessing and promising approach for this modelling.

3.4 Discussions:

In this study, we explored the efficacy of data-driven machine learning (ML) and Physics-Informed Neural Networks (PINNs) for thermal modelling in Wire Arc Additive Manufacturing (WAAM). The data-driven approach aimed to develop a model capable of predicting thermal cycles with high accuracy and minimal computational expense. Utilizing Recurrent Neural Networks (RNNs), the model was trained on simulation data to predict temperatures at specific coordinates and times, demonstrating initial high accuracy but diverging over longer periods without iterative corrections. This may happen due to failure by model on accurate relative torch position computations and may be more complex network is needed. Conversely, the PINN approach integrated the governing physical principles of heat transfer into the neural network, ensuring predictions adhered to physical laws. For the laser-directed energy deposition (L-Ded) process, the PINN model achieved an average prediction error of 16.34% which shows the model can be further improved by incorporating temperature dependent properties. In contrast, the WAAM process initially showed a prediction error of 23.25%, which improved to 20.56% when temperature-dependent properties were considered. The model is performing well in Heating part of the thermal cycle, and from there it was not able to capture the exact cooling phase dynamics where exactly the reheating of the previous part of the track takes place due to which the predictions curves not so accurate although it follows the trend. This is where the Hybrid model can help by using some data support especially where the

model fails to converge or capture the exact dynamics. In this study, we have implemented the hybrid model by extracting around 174 data points by random sampling and incorporated with loss function which resulted in drastic reduction in average percentage error to 9.3%, so Hybrid models underscore the potential of combining physics-informed and data-driven methods for superior thermal modelling. Future research should extend these models to more complex scenarios, including multilayer builds and generalized domain variations, to enhance their robustness and applicability in real-world manufacturing.

Chapter 4

Future work

Data-Driven Approach:

- One of future work can be to integrate the data driven approach with differential matrix forms from FVM formulation as an extra loss term
- Development of more complex models and carryout robust hyperparameter tuning can aid this problem.

PINN Approach:

- **Laser-Directed Energy Deposition (L-DED) Process:**
 - Train the network by incorporating the temperature dependent properties.
- **WAAM Process:**
 - The model is performing well in Heating part of the thermal cycle, and from there it is not exactly able to capture the cooling phase of the cycle where exactly the that point undergoes reheating due to which the predictions curves not so accurate although it follows the trend.
 - Sequential modelling and Physics based Transfer learning may help to overcome this problem.

Hybrid PINN Model:

- This approach seems to be promising for this problem and surely further improved by manipulating the network parameters and Hyperparameter Tuning.

One of appreciable future work is to develop a Generalized domain size variable model

- Extend the model for multilayer build and multipath beads
- One more appreciable future work may be to develop a automatic domain sampling algorithm for custom distribution of domain

Code and Data availability:

The code used for the study can be found at:

https://github.com/Jagadeesh-23/M.Tech_thesis.git

References

- [1] Alagha, Ali & Hussain, Shahadat & Zaki, Wael. (2021). Additive manufacturing of shape memory alloys: A review with emphasis on powder bed systems. *Materials & Design*. 204. 109654. 10.1016/j.matdes.2021.109654.
- [2] Oh, Wook & Son, Jong & Baek, Gyeong & Shim, Do. (2020). Excess deposition for suppressing interfacial defects induced on parts repaired using direct energy deposition. *The International Journal of Advanced Manufacturing Technology*. 106. 10.1007/s00170-019-04650-w.
- [3] <https://medium.com/@poudelsushmita878/recurrent-neural-network-rnn-architecture-explained-1d69560541ef>
- [4] Xi'an Li, Jiaxin Deng, Jinran Wu, Shaotong Zhang, Weide Li, You-Gan Wang, Physical informed neural networks with soft and hard boundary constraints for solving advection-diffusion equations using Fourier expansions, *Computers & Mathematics with Applications*, Volume 159, 2024, Pages 60-75, ISSN 0898-1221, <https://doi.org/10.1016/j.camwa.2024.01.021>.
- [5] E. A. Bonifaz, "Modelling of Thermal Transport in Wire + Arc Additive Manufacturing Process," in ICCS, Switzerland, 2019.
- [6] R.F.V. Sampaio, J.P.M. Pragana, I.M.F. Bragança, C.M.A. Silva, C.V.Nielsen, P.A.F. Martins, Modelling of wire-arc additive manufacturing – A review, *Advances in Industrial and Manufacturing Engineering*, Volume 6, 2023, 100121, ISSN 2666-9129, <https://doi.org/10.1016/j.aime.2023.100121>.

- [7] H. Zhao, G. zhang, Z. Yin and L. Wu, "A 3D dynamic analysis of thermal behavior during single-pass multi-layer weld-based rapid prototyping," Journal of Materials Processing Technology, p. 8, 2011.
- [8] Bowman, Brett & Oian, Chad & Kurz, Jason & Khan, Taufiquar & Gil, Eddie & Gamez, Nick. (2023). Physics-Informed Neural Networks for the Heat Equation with Source Term under Various Boundary Conditions. Algorithms. 16. 428. 10.3390/a16090428.
- [9] Lagaris, Isaac & Likas, Aristidis & Fotiadis, Dimitrios. (1998). Artificial neural networks for solving ordinary and partial differential equations. IEEE Transactions on Neural Networks. 9. 987-1000. 10.1109/72.712178.
- [10] Navid Zobeiry, Keith D. Humfeld,A physics-informed machine learning approach for solving heat transfer equation in advanced manufacturing and engineering applications, Engineering Applications of Artificial Intelligence,Volume 101,2021,104232, ISSN 0952-1976,
- [11] Voigt, Jorrit & Möckel, Michael. (2022). Modelling dynamic 3D heat transfer in laser material processing based on physics informed neural networks. EPJ Web of Conferences. 266. 10.1051/epjconf/202226602010.
- [12] Zhu, Qiming & Liu, Zeliang & Yan, Jinhui. (2021). Machine learning for metal additive manufacturing: predicting temperature and melt pool fluid dynamics using physics-informed neural networks. Computational Mechanics. 67. 10.1007/s00466-020-01952-9.
- [13] Shuheng Liao, Tianju Xue, Jihoon Jeong, Samantha Webster, Kornel Ehmann, Jian Cao, "Hybrid thermal modeling of additive manufacturing processes using physics-informed neural networks for temperature 56 prediction and parameter identification.," Computational Mechanics, p. 14, 2022.
- [14] Li, Chao & Song, Yingming & Zhang, Zehuan & Mao, Jie & Yuan, Weiwei & Wang, Bo. (2021). A Novel and High-Precision Method for Calculating the γ -Ray Build-Up Factor for Multilayer Shields. Science and Technology of Nuclear Installations. 2021. 1-15. 10.1155/2021/8860762.
- [15] Shilin Li, Gang Wang, Yuelan Di, Liping Wang, Haidou Wang, Qingjun Zhou, A physics-informed neural network framework to predict 3D temperature field without labeled data in process of laser metal deposition, Engineering Applications of

Artificial Intelligence, Volume 120, 2023, 105908, ISSN 0952-1976,
<https://doi.org/10.1016/j.engappai.2023.105908>.

[16] Pham, Thinh & Manh Cuong, Bui & Le, Van Thao & Bui, Vuong & Tran, Xuan. (2023). Effects of Process and Heat Source Parameters on Temperature Evolution in Thin-wall Wire Arc Additive Manufacturing using Explainable Deep Learning. Science and Technology Development Journal. 26. 10.32508/stdj.v26i4.4190.